Main Manuscript for

Unexpected anthropogenic emission decreases are required to explain recent atmospheric mercury concentration declines

Aryeh Feinberg[a*], Noelle E. Selin[a,b], Christine F. Braban[c], Kai-Lan Chang[d,e], Danilo Custódio[f], Daniel A. Jaffe[g,h], Katriina Kyllönen[i], Matthew S. Landis[j], Sarah R. Leeson[c], Winston Luke[k], Koketso M. Molepo[l], Marijana Murovec[m], Michelle G. Nerentorp Mastromonaco[n], Katrine Aspmo Pfaffhuber[o], Julian Rüdiger[p], Guey-Rong Sheu[q], and Vincent L. St.Louis[r]

[a] *Institute for Data, Systems, and Society, Massachusetts Institute of Technology, Cambridge, MA 02139, USA*

[b] *Department of Earth, Atmospheric, and Planetary Sciences, Massachusetts Institute of Technology, Cambridge, MA 02139, USA*

[c] *UK Centre for Ecology & Hydrology (UKCEH), Penicuik, Midlothian EH26 0QB, UK*

[d] *Cooperative Institute for Research in Environmental Sciences, University of Colorado, Boulder, CO 80309-0401, USA*

[e] *NOAA Chemical Sciences Laboratory, Boulder, CO 80305, USA*

[f] *Max-Planck-Institut für Biogeochemie, D-07745 Jena, Germany*

[g] *School of STEM, University of Washington Bothell, Bothell, WA 98011, USA*

[h] *Department of Atmospheric Sciences, University of Washington Seattle, Seattle, WA 98195, USA*

[i] *Finnish Meteorological Institute, Helsinki 00560, Finland*

[j] *United States Environmental Protection Agency, Office of Research and Development, Research Triangle Park, NC 27711, USA*

[k] *NOAA/Air Resources Laboratory, College Park, MD 20740, USA*

[l] *Institute of Coastal Environmental Chemistry, Helmholtz Zentrum Hereon, 21502 Geesthacht, Germany*

[m] *Slovenian Environment Agency, Environment and Nature protection Office, Air Quality Division,1000 Ljubljana, Slovenia*

[n] *IVL Swedish Environmental Research Institute, SE-411 33 Gothenburg, Sweden*

[o] *NILU, 2027 Kjeller, Norway*

[p] *Air Monitoring Network, German Environment Agency, 63225 Langen, Germany*

[q] *Department of Atmospheric Sciences, National Central University, Taoyuan 320, Taiwan*

[r] *Department of Biological Sciences, University of Alberta, Edmonton, AB T6G 2E9, Canada*

*Correspondence to: arifeinberg@gmail.com (A.F.)

Author Contributions: A.F. and N.E.S. designed the research. K.-L.C. advised the implementation of statistical methods. C.F.B., D.C., D.A.J., K.K., M.S.L., S.R.L., W.L., K.M.M., M.M., M.G.N.M., K.A.P., J.R., G.-R.S., and V.L.S.L. contributed Hg observation data. A.F. performed the analysis and wrote the manuscript under the supervision of N.E.S., with inputs and discussion from all authors. Author order is alphabetical following the second author, N.E.S.

Competing Interest Statement: The authors declare no competing interests.

Classification: Physical Sciences/Earth, Atmospheric, and Planetary Sciences

Keywords: mercury trends; anthropogenic emissions; atmospheric observations; Minamata Convention on Mercury; biogeochemical box model; chemistry-transport model.

This PDF file includes:

Main Text
Figures 1 to 4
Table 1

Abstract

Anthropogenic activities emit ~2000 Mg yr^{-1} of the toxic pollutant mercury (Hg) into the atmosphere, leading to long-range transport and deposition to remote ecosystems. Global anthropogenic emissions inventories report increases in Northern Hemispheric (NH) Hg emissions during the last three decades, in contradiction with the observed decline in atmospheric Hg concentrations at NH measurement stations. Many factors can obscure the link between anthropogenic emissions and atmospheric Hg concentrations, including trends in the re-emissions of previously released anthropogenic ("legacy") Hg, atmospheric sink variability, and spatial heterogeneity of monitoring data. Here we assess the observed trends in gaseous elemental mercury (Hg^0) in the NH and apply biogeochemical box modeling and chemical transport modeling to understand the trend drivers. Using linear mixed effects modeling of observational data from 51 stations, we find negative Hg^0 trends in most NH regions, with an overall trend for 2005–2020 of -0.011 ± 0.006 ng m^{-3} yr^{-1} (±2 SD). In contrast to existing emission inventories, our modelling analysis suggests that NH anthropogenic emissions must have declined by at least 140 Mg yr^{-1} between the years 2005 and 2020 to be consistent with observed trends. Faster declines in 95th percentile Hg^0 values than median values in Europe, North America, and East Asian measurement stations corroborate that the likely cause is a decline in nearby anthropogenic emissions rather than background legacy re-emissions. Our results are relevant for evaluating the effectiveness of the Minamata Convention on Mercury, demonstrating that existing emissions inventories are incompatible with the observed Hg^0 declines.

Significance statement

Mercury (Hg) is a global pollutant that bioaccumulates to toxic concentrations along the food chain. Anthropogenic Hg inventories suggest increasing global emissions over recent decades, which is at odds with observed declines of atmospheric Hg concentrations in the Northern Hemisphere (NH). We use statistical and process-based modeling to rule out the possibility that NH anthropogenic emissions of Hg could have increased while atmospheric Hg concentrations declined. This implies that anthropogenic emissions of Hg have very likely declined in recent years. This work informs the effectiveness evaluation of the international Minamata Convention on Mercury. Further research is required to better link emission changes with measured concentrations so that the specific causes of global Hg trends can be identified.

Main Text

Introduction

The global Minamata Convention on Mercury is a multilateral environmental agreement that aims to "protect human health and the environment from anthropogenic emissions and releases of mercury", a neurotoxic pollutant (1). As mercury (Hg) is volatile and long-lived (~6 months) in the atmosphere (2), trends in atmospheric mercury concentrations are one of the proposed indicators that will be used to evaluate the Convention's effectiveness (3). However, linking trends in Hg concentrations and anthropogenic emissions is not a straightforward process. The major anthropogenic emissions sources of Hg, including artisanal and small-scale gold mining (ASGM), coal combustion, and industrial processes, are distributed heterogeneously across the globe (4, 5). At the same time, legacy re-emissions of historical anthropogenic mercury from soils, freshwater, wildfires, and oceans are diffuse background sources, which are thought to make up a larger fraction of the overall Hg source fluxes (60% for legacy re-emissions vs. 27% for primary anthropogenic) (6). Atmospheric Hg monitoring stations are also not evenly distributed globally, with more stations located in North America and Europe (7), and they cover different time periods. Therefore, statistical modeling is necessary to maximize the information present in atmospheric Hg records (8), while mechanistic modeling helps connect observed Hg concentrations with their drivers, i.e., emissions, chemical transformations, transport, and deposition (7).

The large-scale trends of atmospheric Hg over the last three decades have been under recent debate. Bottom-up inventories show increasing global anthropogenic emissions since the 1990s (5, 9, 10), which, all else being equal, should increase atmospheric Hg concentrations. However, in North America and Europe, measured gaseous elemental mercury (GEM: Hg^0) concentrations have generally been declining since continuous measurements began in the 1990s (7, 11–14). There is a clear need to understand this contradiction and evaluate past trends of Hg emissions, especially after the adoption of the Minamata Convention in 2013. Zhang et al. (7), the most recent study to evaluate the consistency between emission inventories and atmospheric observations using the chemical-transport model GEOS-Chem, analyzed available data through 2014. Their comparison between the model and measurements from North America and Europe led the authors to conclude that anthropogenic Hg emissions declined by ~30% between 1990 and 2010, due to weaker increases of Hg emissions from ASGM and strong declines in Hg emissions from commercial products (7). More recent measurements from East Asian stations have also reported declines in atmospheric Hg (15–18). Long term measurements from the Southern Hemisphere (SH) remain scarce, with the latest results from the observation stations Cape Point and Amsterdam Island showing insignificant trends between 2012–2017 (19). Alternative hypotheses have been proposed to explain the decline in atmospheric Hg in the Northern Hemisphere (NH) while anthropogenic emissions rise, including increased elemental mercury (Hg^0) uptake by vegetation (20) and declining Hg emissions from ocean legacy re-emissions due to reduced anthropogenic inputs after the 1970s (21, 22). However, a decline in legacy emissions of Hg is difficult to reconcile with biogeochemical box models, which suggest that legacy Hg emissions generally increase if anthropogenic emissions are constant or increasing (23).

Here, we perform trend analyses on a compiled NH dataset (1992-2022) of ambient Hg^0 measurements and conduct biogeochemical box model and GEOS-Chem chemistry-transport model simulations to identify emissions trends that would be compatible with observed concentration trends. We focus on Hg^0 measurements rather than gaseous oxidized mercury (GOM) and wet deposition measurements, as past measurements of GOM may have been biased low (24) and wet deposition is more strongly affected by meteorological variability (25). We derive trends not only in the mean or median changes in Hg^0 but also in other statistical quantiles (e.g., 95th percentile) using quantile regression, which can provide additional information regarding the drivers of trends.

Results and Discussion

Regional trends in observed Hg^0 (1992–2022). We analyzed Hg^0 data from 51 long-term monitoring stations across the NH (Fig. 1). To calculate trends over wider regions, we aggregated stations based on Intergovernmental Panel on Climate Change (IPCC) regions (26) and calculated overall trends using linear mixed effect modeling (Fig. 2A–K and Table S1). Overall trends for all NH regions except Northwestern North America are declining over the available measurement periods between 1992 and 2022, with declines ranging between -0.007 and -0.035 ng m^{-3} yr^{-1} (concentration units refer to standard temperature and pressure, STP). Northwestern North America (Fig. 2J) is the only NH region to show a positive trend, but this region only includes one measurement site (Little Fox Lake, Yukon, Canada). Two possible hypotheses for the positive trend in Little Fox Lake have been suggested: increasing transport from East Asia or increasing wildfire frequency in Western Canada (12). However, in our analysis, the East Asian region also shows declining Hg^0 concentrations over 2006–2022 (trend -0.023 ± 0.005 ng m^{-3} yr^{-1}) (Fig. 2H). Declines have also been observed in other published shorter term measurement records from China (17, 18, 27, 28). For the regions with more available measurement stations, including Eastern North America (ENA, n = 19) and Northern Europe (NEU, n = 13), we tested a nonlinear method of obtaining an overall regional trend using generalized additive models (GAM) (8). The derived regional trends are robust, as both the linear and nonlinear approaches of deriving regional trends yield similar declines in these regions for 2005–2020 (-0.01 to -0.02 ng m^{-3} yr^{-1}) (Supplemental Information, SI, Fig.

S4). We have also calculated similar regional trends when conducting a sensitivity test where the analysis of site data is limited to the 2005–2020 period (SI Fig. S5 and Table S3).

We find an overall NH Hg^0 decline of -0.011 ± 0.006 ng m^{-3} yr^{-1} (± 2 standard deviations) for the period 2005–2020 (Fig. 2L), calculated by averaging regional trends (Fig. 2A–K) weighted by the areas of corresponding IPCC regions. By first aggregating site trends by region, we reduce inherent biases from the uneven spatial distribution of sites (i.e., biasing toward the trends of Eastern North America and Europe) (SI Fig. S2). Our results largely agree with a previous trend assessment conducted on data from 1990–2014 (7), which found regional declines in Hg^0 of -0.6 to -2% yr^{-1} (approximately corresponding to -0.01 to -0.03 ng m^{-3} yr^{-1}). The current work benefits from improved statistical techniques to combine information from multiple sites and a larger number of stations and regions covered in more recent time periods. We have not included an analysis of SH regional trends in the current work due to the sparse coverage of SH long-term monitoring stations (Fig. 1). From published information, two SH monitoring stations (Cape Point, South Africa and Amsterdam Island) do not show significant trends during the 2012–2017 period, while Cape Point shows a positive trend of ~0.008 ng m^{-3} yr^{-1} over 2007–2017 (19). As the NH has a wider dataset of Hg^0 time series and is the principal hemisphere for anthropogenic emissions, we proceed with constraining Hg budget trends based on the NH Hg^0 trend.

Constraining emissions trends for 2005–2020. We ran 2 × 10^5 scenarios in a biogeochemical box model for 2005–2020, varying 19 Hg budget parameters including the trends in anthropogenic emissions and releases, the response of legacy emissions to recent and historical anthropogenic inputs, emissions speciation trends, and the atmospheric Hg lifetime (Table S4). Figure 3A compares the distributions of simulated Hg^0 trends for specific trends in anthropogenic emissions, given the uncertainty ranges of all other factors. Note that emissions fluxes are reported in Mg yr^{-1}, and thus trends in these fluxes are expressed as Mg yr^{-2}. Our best estimate for the observed 2005–2020 trend in surface NH Hg^0 is -0.011 ± 0.006 ng m^{-3} yr^{-1}. However, to account for potential differences between NH surface and whole troposphere trends (SI Section S3.1) we assumed an extended uncertainty range for NH tropospheric Hg^0 trends from -0.017 to -0.004 ng m^{-3} yr^{-1} (error bar in Fig. 3A).

The uncertainty range for observed NH troposphere Hg^0 trends is compatible (>5% overlap in histogram) only with anthropogenic emission trends that are declining by more than -9 Mg yr^{-2} (Fig. 3A). Stronger declines in anthropogenic emissions lead to more overlap between the simulated and observed trend ranges, yet they become more difficult to reconcile with existing bottom-up inventories. Our box modeling analysis is consistent with a previous emissions trend estimate based on 1990–2010 observations (610 Mg yr^{-1} total difference; -30.5 Mg yr^{-2} trend) (7). The positive NH anthropogenic emissions trend estimated by the Streets et al. (10) inventory for 2005–2015 (34 Mg yr^{-2}), should result in NH Hg^0 increases on the order of 0.09 ng m^{-3} yr^{-1}, with no overlap in the observed trend range. Other global inventories differ in terms of their temporal coverage, yet the EDGAR v4.tox2 inventory estimates an increase of 54 Mg yr^{-2} over 2005–2012 in the NH (9) and the AMAP/UNEP inventory estimates an NH increase of 44 Mg yr^{-2} between 2010 and 2015 (5). The EDGAR v8.1_toxHg inventory, which was recently released but remains in draft form for speciation estimates (29), shows an NH increase of 35 Mg yr^{-2} for 2005–2020 (Fig. S14), We conclude that current bottom-up inventories of anthropogenic Hg emissions are inconsistent with the declines in observed NH Hg^0 for 2005–2020.

Previous studies (21, 22) have hypothesized that NH Hg^0 may be decreasing due to broad-scale declines in legacy emissions, even as anthropogenic emissions increase or stay constant. However, our biogeochemical box model analysis illustrates that it is very unlikely for legacy emissions to decrease if recent (2005–2020) anthropogenic emissions are not also decreasing. Even if anthropogenic emissions stay constant, legacy emissions will grow due to the increasing supply of Hg (23). This effect means that

in the case of an anthropogenic emissions trend of zero, the median predicted Hg^0 trend will be positive due to positive trends in re-emissions (Fig. 3A and Fig. S7B). The trend in anthropogenic emissions must be below -8 Mg yr^{-2} for the median predicted Hg^0 trend to become negative (Fig. S7B). We explored the potential impacts of errors in the historical emission and release inventories on the recent re-emissions trend (Fig. S8). If we assume underestimates in 1970 emissions and releases, when Hg discharges were at their peak (30, 31), the recent re-emissions trend would be more negative (Fig. S8A). However, the degree to which the potential error in 1970 emissions affects the 2005–2020 re-emissions trend is smaller than the impacts of more recent errors (1990, 2000), and a factor of ~15 smaller than the influence of contemporary (2005–2020) anthropogenic emissions and releases trends (Figs. S8F and G). Therefore, although historical emissions and releases from earlier decades (>30 years) can affect the recent re-emissions trend, the dominant factor for the recent re-emissions trend will be recent trends (<15 years) in anthropogenic Hg inputs to the environment. Our results take into account the uncertainties in the multiple lifetimes of legacy Hg in the surface environment (Table S4).

We explored the role of trend drivers other than anthropogenic inputs by repeating the sampling of the box model throughout the parameter space, accounting for additional causes. If the oxidation lifetime of Hg^0 declined between 2005–2020, it can become easier to reconcile the observed Hg^0 decline with positive anthropogenic emissions trends (Fig. 3B). However, the oxidation lifetime of Hg^0 would have to decline by 13% for at least a 5% likelihood of positive anthropogenic emissions trends (i.e., when the oxidation lifetime declines by 13% over 2005–2020, 5% of the simulations that are within the observed NH Hg^0 trend range have positive NH anthropogenic emissions trends). A hemispheric decrease in the oxidation lifetime of this magnitude would be surprising for the 2005–2020 period, as modeling estimates for the methane (CH_4) lifetime suggest only 9% declines over the longer period of 1980–2014, driven by increases in hydroxyl radical (OH) concentrations (32). In addition, the two-step Hg oxidation chemistry will be affected by other oxidants as well, including ozone, bromine radicals, and nitrogen oxides (2, 33–35). A recent study has highlighted the role of anthropogenic short-lived halogens in continental Hg oxidation, with more work required to understand their trends (36). Oxidants impacted by anthropogenic pollution sources have likely trended differently in different regions, and therefore are likely not the main factor between the consistent declines seen across the NH. An increased oxidation rate would also have enhanced the sink of Hg through wet deposition, as oxidation converts insoluble Hg^0 to soluble species. However, previous studies have identified overall declines in wet deposition of Hg over North America (13, 14, 37) and Europe (5).

Another potential factor is the increase in terrestrial primary production through global greening, which Jiskra et al. (20) estimated increased the NH dry deposition of Hg^0 to vegetation by 140 Mg yr^{-1} between 1990 and 2010; this corresponds to a decrease of approximately 13% in their estimated Hg^0 lifetime due to vegetation uptake. However, the NH Hg^0 dry deposition lifetime would have to decline by more than 19% between 2005 and 2020 to yield a 5% likelihood of positive anthropogenic emissions trends (Fig. 3C). A change of this magnitude to vegetation uptake during 2005–2020 is unrealistic, as our GEOS-Chem simulation for that time period shows only a 3% decline in the Hg^0 dry deposition lifetime due to vegetation changes (Fig. S10). Other climate change factors can play a role in recent legacy emissions trends, like release of Hg from melting permafrost (38), changes to ocean evasion of Hg^0 through warming, acidification, and wind speed changes (39), decreased sea ice coverage allowing further Hg^0 evasion (40), and enhanced wildfire emissions (41). These identified climate feedbacks, however, tend to increase legacy Hg re-emissions, and thus could not explain why anthropogenic emissions in bottom-up inventories increase while Hg^0 trends decline. Although further research into these factors is required to reduce uncertainties in recent trend drivers, our conclusion remains that it is very unlikely that NH anthropogenic emissions could have increased or even stayed constant over 2005–2020, with the Hg^0 declines observed over this period in the NH.

Spatial and quantile variability of Hg^0 trends. Although the box model is useful for constraining overall hemispheric trends, it cannot capture the spatial heterogeneity of these trends driven by variability in sources, sinks, and transport. We ran simulations (Table 1) in the 3-D chemical-transport model GEOS-Chem (42, 43) to investigate different emissions scenarios over the 2005–2020 period and calculated mean trends in NH Hg^0 using area-weighted averaging of observed regions (Fig. 4A). The BASE simulation, including anthropogenic emissions increases according to Streets et al. (10) for 2005–2015 with constant emissions after 2015, shows an increase in NH Hg^0 of 0.006 ng m^{-3} yr^{-1}. In the BASE+LEG simulation, we considered the feedback of legacy emissions to increasing anthropogenic emissions, leading to a stronger increase of 0.010 ng m^{-3} yr^{-1} in NH Hg^0. Echoing the box modeling results, we thus find that increases in anthropogenic emissions found in existing inventories is inconsistent with the observed trends in NH Hg^0, -0.011 ± 0.006 ng m^{-3} yr^{-1}. Replacing Chinese emissions within BASE by the regional inventory trend from Zhang et al. (44), the ZHANG23 simulation shows a slight negative trend in NH Hg^0 (-0.001 ng m^{-3} yr^{-1}). We simulated two further scenarios for a decreasing NH emissions trend: DEC_ANT_NH, where an additional decline of 23 Mg yr^{-2} in the NH is imposed on top of the ZHANG23 scenario, and DEC_LEG_ONLY, which considers declining ocean re-emissions of Hg in the NH and SH. Both of these emission scenarios are within uncertainties of the observed trend in mean NH Hg^0 (DEC_ANT_NH: -0.009 ng m^{-3} yr^{-1}; DEC_LEG_ONLY: -0.012 ng m^{-3} yr^{-1}). Since it is difficult to understand the causes of the Hg^0 decline based on the mean hemispheric trend alone, we also assess the spatial and quantile variations in trends.

We use quantile regression to assess trends in the observed median (P50) and 95th percentile (P95) deseasonalized daily Hg^0 values. Fig. 4B maps the simulated P50 trends in BASE+LEG, showing increasing concentrations across the globe, in disagreement with 8 of the 9 plotted stations (>13 years observed between 2005 and 2020), which show declines. The difference between P95 trends and P50 trends (Fig. 4C) correlates with the change in anthropogenic emissions between 2005 and 2020 (Fig. S11). BASE+LEG simulates P95 declining more than P50 in Eastern North America and Central Europe (areas of emissions decreases in the global inventory), while P95 increases more than P50 in East Asia and South Africa (areas of emissions increases). Available high-resolution measurement records confirm the simulated P95 – P50 trends in Eastern North America (Egbert and Kejimkujik) and Europe (Mace Head, Schmücke, and Pallas), yet they also show declines in East Asia (Cape Hedo). In the simulations where Chinese emissions decline between 2005 and 2020 (ZHANG23 and DEC_ANT_NH), the simulated P95 – P50 trends agree with observations at Cape Hedo, showing negative values (Figs. 4E and S12D). In the DEC_LEG_ONLY simulation, declining legacy emissions lead to agreement with the observed P50 NH Hg^0 trends (Fig. 4F), but the P95 – P50 trends remain similar to BASE+LEG and are opposite in sign to Cape Hedo observations (Fig. 4G). Therefore, despite showing similar P50 trends (Figs. 4D and F) in NH Hg^0, DEC_ANT_NH and DEC_LEG_ONLY can be distinguished by simulated patterns in quantile trends. The current results support findings from Hg measurement studies in the 1990s (45, 46), which suggested that reductions in observed extreme concentrations could be useful indicators for regional emissions changes. Incorporation of quantile trends as constraints in Hg modeling can thus help maximize the information provided by high resolution monitoring stations.

Implications for the drivers of atmospheric Hg trends.

Observed Hg^0 is generally declining in most NH regions, with an estimated hemispheric trend of -0.011 ± 0.006 ng m^{-3} yr^{-1} for 2005–2020. By testing a large ensemble of parameters using box modeling and comparing with available measurements of atmospheric concentrations, we showed that NH anthropogenic emissions likely declined by more than -140 Mg yr^{-1} (-9 Mg yr^{-2}) over this period (Fig. 3A). This result is at odds with existing anthropogenic emissions inventories (5, 9, 10, 29), which all show NH increases of larger than 34 Mg yr^{-2}. Thus, there is a potential gap of 43 Mg yr^{-2} (~650 Mg yr^{-1}) between estimated anthropogenic emissions trends from inventories and trends expected from observed Hg^0

trends. This gap could quantitatively be impacted (in both directions) by factors like the Hg^0 oxidation lifetime and vegetation sink, yet it is unlikely to be substantially reduced (Fig. 3B–C). Our ZHANG23 simulation showed that this gap could be partially explained by incorrect Chinese emissions trends in the global emission inventory, with Chinese national inventories including more detailed information on air pollution control device efficiencies (44, 47, 48). The hypothesis of declining Chinese emissions is supported by the observed decline in P95 Hg^0 concentrations at Cape Hedo (Fig. 4E), along with observed declines in mean Hg^0 values from other East Asian stations (Fig. 2H). However, additional declines in anthropogenic emissions across the NH were necessary to match the magnitude of the observed trend in the DEC_ANT_NH simulation. The gap between inventories and measurement-derived emissions trends could be due to the large uncertainties associated with several anthropogenic emissions sources. For example, ASGM is currently thought to be the largest yet highly uncertain source (globally 775 Mg yr^{-1} in 2015) of anthropogenic Hg emissions (10), and estimated trends in this source can differ depending on whether it is estimated to change with time following different proxies such as gold demand or poverty (10, 49). High uncertainties are also linked with emissions from Hg-containing products (globally 436 Mg yr^{-1}) (10), as the magnitudes of historically produced Hg are large (~1000 Gg) and emissions factors as well as timescales are uncertain (50). Measurement constraints are limited, and our five tested GEOS-Chem simulations are not intended to cover the entire range of uncertainty in emissions scenarios, so we cannot further identify the source types responsible for the discrepancy between emissions inventory and observed trends. Nevertheless, both our box and GEOS-Chem modeling analyses suggest that a decline in legacy emissions in the absence of anthropogenic emissions reductions is unlikely given our understanding of the Hg cycle and measured quantile trends.

The amount of uncertainty in anthropogenic emissions and biogeochemical cycling of Hg emphasizes the need for continued assessment of inventories and models based on available observations and emerging constraints like Hg isotopes (51). Expansion of current monitoring networks in strategic locations and increased public availability of data would be valuable for trend quantification and attribution to sources. For example, existing SH measurement locations are largely influenced by marine rather than anthropogenic sources (52, 53), with no long-term measurement stations located nearby ASGM activities (Fig. 1). We focused here on trends in Hg^0 in the NH due to the increased prevalence of NH anthropogenic emissions and monitoring, but further monitoring of atmospheric Hg in the SH is essential for constraining trends in Hg sources. For example, major differences between the simulated DEC_ANT_NH and DEC_LEG_ONLY median trends occur in the SH (Fig. 4). Passive samplers (54) can enable economical Hg monitoring in remote locations, yet active continuous sampling will continue to deliver the benefits of higher time resolution (e.g., atmospheric dynamics, source identification) compared to passive samplers (~monthly resolution). Here we showed that the trends in the statistical distribution of Hg^0, which can only be facilitated by active sampling methods, are a useful indicator of which sources are changing. As more data become available from sites measuring GOM using a new generation of methods with smaller biases (55, 56), it will be possible to analyze long term trends in different fractions of atmospheric Hg, providing further information about source changes. Reduced-form models (57, 58) and tools to produce emissions inventories from socioeconomic data more quickly (59), which have been applied extensively in the climate and air pollution fields, can enable more up-to-date evaluations of the latest Hg trends and drivers. Improvements in Hg models will be essential for further analysis of Hg trends, for example refining the response of legacy re-emissions to anthropogenic emissions scenarios and global change factors. The planned analysis to support the Minamata Convention effectiveness evaluation will advance this approach by investigating the drivers of Hg trends in multiple Hg models (60). As declining atmospheric Hg inputs to ecosystems can directly impact concentrations of Hg in biota (61), understanding the trends in atmospheric Hg burden is essential for better predictions of how Hg pollution will evolve under future regulatory control scenarios and climate change.

Materials and Methods

Atmospheric mercury observations. Atmospheric mercury (Hg) occurs as different species: the volatile species gaseous elemental mercury (GEM: Hg^0), the soluble, shorter-lived species gaseous oxidized mercury (GOM: Hg^I and Hg^{II}), and particulate-bound mercury (Hg^P). We compiled data from 51 stations which have more than 6 years of measurements of Hg^0 or total gaseous mercury (TGM = Hg^0 + GOM) in the period 1992 to 2022 (Table S1). Measurements reporting TGM are likely more representative of Hg^0 due to low biases in capturing GOM (62, 63), and therefore we do not differentiate between TGM and Hg^0 measurements. We consider all measurements as Hg^0 when comparing to modeled quantities. We have also tested whether the trend results are similar if modeled TGM data are analyzed instead of Hg^0 and the differences are minor. We analyzed data from multiple measurement networks: the US National Atmospheric Deposition Program's (NADP) Atmospheric Mercury Network (AMNet) (64), Canadian Air and Precipitation Monitoring Network (CAPMoN) (37), European Monitoring and Evaluation Programme (EMEP) (65), Global Mercury Observation System (GMOS) (66), Ministry of Environment Japan (MOEJ) (15), Ministry of Environment (MOENV) Taiwan (16), and the Experimental Lakes Area (67). We also included a Mauna Loa measurement dataset from the US EPA from 2002 to 2009 (68, 69), which later transitioned into an AMNet site. Most TGM and Hg^0 measurements were made with Tekran Instruments Corporation (Toronto, Canada) Models 2537A/B/X systems, which capture ambient Hg by gold trap amalgamation, subsequently thermally desorbing this accumulated Hg to be detected by Cold Vapour Atomic Fluorescence Spectrometry (CVAFS) (69). Two sites in the EMEP network (Iskrba after 2017 and Lahemaa) employed Lumex Instruments (St. Petersburg, Russia) Model RA-915 mercury analyzers, which detect Hg^0 through Zeeman Atomic Absorption Spectrometry using High Frequency Modulated light polarisation (ZAAS-HFM) (70). Before 2017, TGM was measured at Iskrba with Mercury Instruments Analytical Technologies (Karlsfeld, Germany) Model UT-3000 analyzers using cold vapor atomic absorption spectroscopy (CVAAS). All the continuous TGM and Hg^0 measurements are made at 5–15 min intervals, which are averaged and reported hourly. Measurements from Zeppelin Station (before 2000), Birkenes (before 2010), Lista, Råö, Bredkälen, Hallahus, and Pallas (the measurements from IVL, Swedish Environmental Research Institute) were made manually with a gold trap sampling technique (71). Data at lower frequencies (manual sites and the Auchencorth Moss and Iskrba timeseries) were used to compute monthly mean statistics for timeseries. At the sites with high-frequency measurements, daily mean values were calculated and used to compute means for all months with at least 10 daily values. All measurement and modeling data for Hg^0 is reported in units of ng m^{-3} yr^{-1} at standard temperature and pressure (STP, 0 °C and 1 atm).

Statistical methods. Monthly mean data were deseasonalized before trend analysis by fitting each station timeseries with four harmonic terms (72). In order to achieve a better evidence synthesis from individual site data, we focused our statistical analysis on calculating overall trends from wider regions. We chose to aggregate Hg trends based on the IPCC regions (Fig. 1). These regions are standardly used in the atmospheric science community and are designed to have consistent climate features (26), providing advantages over using whole continent or country-based aggregations. There are 61 regions in total; we analyzed trends for 11 regions in the NH where stations measuring Hg over the long term (> 6 years) were available. We aim to derive regionally representative trends by integrating information from all data sources, because individual sites might only provide a partial view of regional variations, as they cover different time periods, come from different measurement networks, include data gaps, and are potentially exposed to unique local sources and sinks. In previous studies on Hg trends, regional timeseries have been calculated by averaging all sites that are available in a particular year (7). However, this approach is biased when sites do not all cover the same time period, since offsets between mean site concentrations can affect the calculated trend results (SI Section S3.2). To address this heterogeneity, we explicitly modeled offsets and trend deviations between sites with linear mixed effects (LME) models (72, 73). Using LME models, a time series can be described with terms representing the consensus trend and

intercept for a region ("fixed effect") and terms representing site-level deviations ("random effect"). Individual sites were modeled using Eq. 1:

$$y_k = a + bt + \alpha_k + \beta_k t \quad \text{(Eq. 1)}$$

where y_k are deseasonalized monthly mean Hg^0 values for each site, a is the regional intercept, b is the regional trend, a_k is the site offset, and β_k is the site deviation in trend. To account for autocorrelation, we assumed that residual errors for each site follow a first-order autoregressive process (AR(1)). We calculated these trends using LME modeling in the R package lme4 (73). For the purposes of LME modeling, EPA and AMNet data for Mauna Loa, as well as Finnish Meteorological Institute (FMI) and Swedish Environmental Research Institute (IVL) data for Pallas, were treated as different sites (as different measurement networks may have offsets). We applied LME modeling to the nine NH regions where multisite data is available. For the two regions (Northwestern North America and the Arctic Ocean) where only one site is available, we calculated generalized least squares (GLS) trends with AR(1) errors on deseasonalized monthly mean values. We chose linear approaches for trend analysis as this follows recommendations for multisite analysis when only a few sites are available for a region (72). We found consistent results between LME trends and nonlinear trends calculated with generalized additive models (GAMs) for regions (Eastern North America and Northern Europe) where a larger number of sites (>12) are available (SI Fig. S4).

We weighted regional trends by the areas of the corresponding IPCC regions to calculate the overall NH trend, which allowed us to compare with box model simulations. The overall NH trend was calculated for 2005–2020, which is the time period with the best availability of data from all 11 regions. The error in the NH trend was calculated through Monte Carlo sampling of regional trends ± 2 standard deviation. Analogous trend calculations were performed for GEOS-Chem simulated Hg^0 values, which showed that NH trends derived from regional weighted averages were more representative of the true NH surface trend than averages of all available sites without regional aggregation (SI Fig. S2).

For sites where high frequency Hg^0 measurements were available, we additionally calculated quantile regression (QR) trends over the 2005–2020 period (74). Other atmospheric chemistry studies (8, 75, 76) have applied QR, as it enables the quantification of trends not only in the mean values but throughout the distribution of the observed quantity. Earlier studies have observed heterogeneous changes in the statistical distribution of atmospheric Hg measurements driven by emissions changes (45, 46), yet these have not been followed up with more modern statistical techniques. We analyzed deseasonalized daily mean values at these sites and calculated trends for 5^{th}–95^{th} percentiles, with errors derived using bootstrapping. We applied the R package quantreg for this analysis (77).

Box model simulations. We used a 3-box model that considers atmospheric Hg^0 and Hg^{II} in two tropospheric boxes (NH and SH) and one stratospheric box (78) to simulate potential scenarios for trends during 2005–2020. We constructed an ensemble of scenarios accounting for uncertainties in the atmospheric Hg lifetime, historical (pre-2005) anthropogenic emissions and releases, recent (2005–2020) anthropogenic emissions and releases, the response of legacy emissions to anthropogenic inputs, and recent (2005–2020) speciation trends. We assigned uncertainty ranges to these 19 parameters (SI Table S4) and sampled 2×10^5 scenarios within this parameter space, using Latin Hypercube Sampling (79).

To address the response in legacy emissions to historical and recent anthropogenic inputs, we applied the effective anthropogenic mercury deposition (EAMD) concept (80). Our approach used two minor adaptations: (1) tracking the effective anthropogenic mercury emissions (EAME) instead of deposition (which leads to offsets of several months in lifetimes); and (2) using a two-term negative exponential model. Given primary emissions or releases of mercury in a specific year (ϵ_i), Eq. 2 calculates the EAME, in a future time *t*:

$$\mathrm{EAME}_i\ (t) = \epsilon_i \left(a_1 \exp\left(-\frac{t}{b_1}\right) + a_2 \exp\left(-\frac{t}{b_2}\right)\right) \quad \text{(Eq. 2)}$$

where a_1 and a_2 are coefficients and b_1 and b_2 are lifetimes representing the quick and slow re-emission processes, respectively. Total legacy emissions (E_{leg}) in the year t were calculated by summing up all EAME_i resulting from previous primary emissions using Eq. 3:

$$E_{\mathrm{leg}}\ (t) = \sum_{i<t} \mathrm{EAME}_i \quad \text{(Eq. 3)}$$

We employed pulse experiments with parameter perturbations in the Hg Global Biogeochemical Box model (GBC) (6, 81) to calculate reasonable ranges for the *a* and *b* parameters (SI Section S4). We pulsed an additional 100 Mg Hg either emitted or released to rivers in 2010 and fit the resultant additional legacy re-emissions until 2110 using Eq. 2. We conducted these pulse experiments on 1000 iterations of the GBC model, varying each of the 40 rate coefficients and parameters within the GBC model within a factor of 2 using Latin Hypercube Sampling. We found that b_1 ranges between 6–15 months for atmospheric emissions and 2–10 months for releases, corresponding to the timescale of atmospheric deposition and re-emission from the surface ocean. The longer lifetime, b_2, ranges between 29–97 years for atmospheric emissions and 1–117 years for releases, corresponding to the timescale of removal of Hg from the atmosphere–surface ocean–subsurface ocean system through transfer to the deep ocean or temporary storage in soils (6). We calculated ranges for the fraction of Hg re-emitted in the short timescale term and the total Hg re-emissions resulting from a pulse, which can be used to calculate a_1 and a_2 in Eq. 2. Although longer time scales (~1000 yr) would be required to model burial of Hg in the deep ocean, Eq. 2 covers the legacy re-emission response in near-future projections (<100 years), while having only 4 parameters as opposed to 40 parameters in the GBC model (80).

Anthropogenic emissions and releases of Hg were taken from the Streets et al. (31) inventory, which covers decadal points over the historical period (1510–2010). We accounted for uncertainties in emissions and releases for recent decadal points (1970, 1980, 1990, 2000, 2010) by applying perturbations between –20% and +40% to these values, which is the suggested emission inventory uncertainty range (10). We interpolated between the decadal points to calculate emissions with yearly resolution between 1510–2005. For 2005–2020, we applied varying linear trends in anthropogenic emissions for both hemispheres, restricting the trend range to ensure non-negative emissions in 2020. The anthropogenic releases for 2005–2020 were calculated based on the historical relationship between emissions and releases trends in the inventory (31), with random perturbations introduced for the hemispheric release trends (Table S4). This procedure yielded 2×10^5 potential timeseries for anthropogenic emissions and releases over 1510–2020. Combining these scenarios with varying sets of legacy parameters (Eq. 2), we calculated the resultant global legacy re-emissions timeseries for 2005–2020 for each of the 2×10^5 scenarios. For simplicity, the distribution of legacy re-emissions by hemisphere was assumed to be constant over 2005–2020 based on the ratio in GEOS-Chem (44% NH, 55% SH; this is similar to the ratio of ocean coverage in the NH and SH). Speciation of the anthropogenic emissions in 2005 was set to 65% Hg^0 and 35% Hg^{II}; we applied a variable linear trend in speciation so that speciation in 2020 ranged between 45% and 85% Hg^0.

We ran the 2×10^5 scenarios in the 3-box model for 2005 to evaluate whether the sampled combinations of emissions and atmospheric Hg lifetimes (ranging between 3–8 months) yield a reasonable Hg burden. We rejected scenarios that yield a 2005 burden in the NH troposphere outside of the range 1600–3300 Mg (corresponding to average tropospheric concentrations of 0.8–1.6 ng m^{-3}). Approximately 10^5 samples passed this constraint, which we then utilized for full 2005–2020 box model runs. We evaluated linear

trends in NH Hg^0 in each of these box model runs and compared these to the inputted total and anthropogenic emission trends for 2005–2020.

To assess the impacts of other non-emissions factors in NH Hg^0 trends, we repeated this procedure accounting for potential trends in Hg^0 dry deposition and oxidation. We re-ran the 2×10^5 scenarios with linear trends in the dry deposition rate coefficient so that the value in 2020 varied between 100% to 170% of its value in 2005. Similarly, we ran 2×10^5 scenarios with the Hg^0 oxidation rate coefficient varying in 2020 between 100% and 200% of its value in 2005.

GEOS-Chem simulations. We ran 3-D atmospheric simulations for the 2005–2020 period in the chemistry-transport model GEOS-Chem. We used version 12.8.1 of the Hg model (42) with improvements in the dry deposition of Hg^0 (78). The model was run globally at 2.0° × 2.5° horizontal resolution and 47 vertical levels up to 0.01 hPa (80 km). The model was forced with offline meteorology from the MERRA-2 product (82). The model treats three species of Hg: elemental mercury (Hg^0), oxidized mercury (Hg^{II}, GOM), and particulate mercury (Hg^P). Oxidation of Hg^0 occurs through a two-step mechanism initiated by atomic bromine (Br), while photoreduction of Hg^{II} occurs in the aqueous phase as a function of the NO_2 photolysis rate and organic aerosol concentrations (42). The reduction rate coefficient (K_RED_JNO2) was set to 2.4 m^{-3} μg^{-1} so that modeled Hg^0 concentrations agree with observed values in 2005. The Hg chemistry in GEOS-Chem has been updated in more recent model versions (v14 onwards), yet the overall atmospheric lifetime and transport of Hg remain similar (2) and the faster computational speed of v12.8.1 facilitates these 16-year simulations. Legacy re-emissions of Hg from the ocean are calculated online (depending on temperature and wind speed) through an air-sea exchange parametrization (83), with concentrations of Hg in the surface ocean taken from a previous ocean general circulation model (MITgcm) simulation (42). Soil legacy emissions are parametrized depending on solar radiation, vegetation cover, and concentrations of Hg in soil (84). The model also considers prompt recycling of Hg^{II} deposited to soils and snow (85), geogenic emissions of Hg^0 (43), and transient emissions of Hg^0 from biomass burning based on GFED v4.1s (86). More comprehensive descriptions of this version of the GEOS-Chem Hg model can be found elsewhere (42, 78).

Five simulations (Table 1) were performed to evaluate spatial heterogeneity in atmospheric Hg trends under different emissions scenarios (SI Fig. S9), which are intended to be illustrative but do not cover the full range of potential scenarios. The BASE case used Streets et al. (10) anthropogenic emissions of Hg for 2005–2015, with 2016–2020 retaining the same emissions pattern as 2015. The BASE+LEG simulation additionally considered the median box modeled trend (Fig. S8F) in NH legacy emissions (+14 Mg yr^{-2}) due to the BASE trend in NH anthropogenic emissions (+23 Mg yr^{-2}) over 2005–2020. This trend in legacy emissions was fully ascribed to the ocean through scaling oceanic sea surface concentrations of Hg (42) to yield the NH trend in legacy emissions. In the ZHANG23 scenario, we replaced the trend in Chinese emissions from BASE with the national inventory in Zhang et al. (44). To distribute Chinese emissions in a consistent way with the Streets et al. (10) inventory, we scaled the emissions for 2005–2020 using the equation:

$$E^{i'}_{\mathrm{ZHANG23}} = E^{i}_{\mathrm{BASE}} \times \frac{E^{i}_{\mathrm{ZHANG23}}}{E^{2005}_{\mathrm{ZHANG23}}} \quad \text{(Eq. 4)}$$

where $E^{i'}_{\mathrm{ZHANG23}}$ are the distributed Chinese emissions applied in the ZHANG23 simulation for year i, E^{i}_{BASE} are the Chinese emissions applied in the BASE, E^{i}_{ZHANG23} are the total Chinese emissions for a specific year in the Zhang et al. (44) inventory, and $E^{2005}_{\mathrm{ZHANG23}}$ are the total Chinese emissions in the Zhang et al. (44) inventory for 2005. In this way, the normalized China trend for 2005–2020 is taken from the

Zhang et al. (44), but emissions magnitudes differ due to differences in 2005 total Chinese emissions between BASE (701 Mg yr^{-1}) and Zhang et al. (44) (466 Mg yr^{-1}). We also adjusted the ZHANG23 trend in NH legacy emissions (+4 Mg yr^{-2}) by scaling ocean concentrations so that it is coherent with the NH anthropogenic emissions trend (-11 Mg yr^{-2}) (Fig. S8F).

To develop a scenario with declining anthropogenic emissions that would be compatible with observed NH Hg^0 trends (DEC_ANT_NH), we imposed an additional 23 Mg yr^{-2} decline for 2005–2020 in the NH. Anthropogenic Hg emissions outside of China were scaled uniformly by year so that the decline is 23 Mg yr^{-2} more than in ZHANG23, for a total anthropogenic trend of -34 Mg yr^{-2} (Table 1). NH legacy emissions (-2 Mg yr^{-2}) were adjusted to be consistent with the DEC_ANT_NH trend in anthropogenic emissions. As a fifth scenario, we explored the possibility where anthropogenic emissions follow BASE, but a major decline (-50 Mg yr^{-2}) in NH ocean legacy emissions occurs (DEC_LEG_ONLY). Thus, the mean NH trends in Hg^0 are similar between DEC_ANT_NH and DEC_LEG_ONLY (Fig. 4A), but the source contribution and spatial distribution varies. In addition, while DEC_ANT_NH includes stagnant overall SH emissions (-2 Mg yr^{-2}), DEC_LEG_ONLY has SH emissions declines (-74 Mg yr^{-2}) due to the scaling of ocean concentrations.

Acknowledgments

This work was funded by the Swiss National Science Foundation through an Early Postdoc.Mobility grant to A.F. (P2EZP2_195424) and a grant (#1924148) from the US National Science Foundation to N.E.S. The EPA through its Office of Research and Development partially funded and contributed to this research. The views expressed in this paper are those of the authors and do not necessarily reflect the views or policies of EPA. It has been subjected to Agency review and approved for publication. Mention of trade names or commercial products do not constitute an endorsement or recommendation for use. The authors acknowledge Environment and Climate Change Canada, the NADP Atmospheric Mercury Network (AMNet), New York State Department of Environmental Conservation, European Monitoring and Evaluation Programme (EMEP), Global Mercury Observation System (GMOS), Ministry of Environment Japan (MOEJ), Ministry of Environment (MOENV) Taiwan, and IISD Experimental Lakes Area for the provision of total gaseous mercury data. The authors would like to acknowledge the following for the funding of the Auchencorth Moss UK site, the UK Department for Environment, Food and Rural Affairs (Defra) and the devolved administrations, via the UK Eutrophying and Acidifying Atmospheric Pollutants (UKEAP) contract and by the Natural Environmental Research Council (NERC) National Capability UK-SCaPE programme. K.-L.C. is supported by NOAA cooperative agreement NA22OAR4320151. We would like to thank David Gay and Ralf Ebinghaus for helpful discussion about available Hg measurements.

Code and Data Availability

Model code, analysis scripts, simulation data, and processed data to reproduce all figures are published in Zenodo (https://doi.org/10.5281/zenodo.12517847) under a CC BY 4.0 license (https://creativecommons.org/licenses/by/4.0/). The full timeseries of observational data are available online from AMNet (https://nadp.slh.wisc.edu/networks/atmospheric-mercury-network/), CAPMoN, (https://www.canada.ca/en/environment-climate-change/services/air-pollution/monitoring-networks-data/canadian-air-precipitation.html, EMEP (https://ebas-data.nilu.no), GMOS (https://sdi.iia.cnr.it/gos4mcat), and MOEJ (https://www.env.go.jp/en/chemi/mcm/monitoringdb2.html). EPA Mauna Loa data related to this manuscript can be found at https://catalog.data.gov/dataset/epa-sciencehub. All other observational data are available upon request to the corresponding measurement network PIs.

References

1. UNTC, Minamata Convention on Mercury (2013).
2. V. Shah, *et al.*, Improved Mechanistic Model of the Atmospheric Redox Chemistry of Mercury. *Environ. Sci. Technol.* **55**, 14445–14456 (2021).
3. UNEP/MC/COP.3, "Proposed indicators for evaluating the effectiveness of the Minamata Convention, by article. Annex I to decision MC-3/10." (2020).
4. F. Steenhuisen, S. J. Wilson, Development and application of an updated geospatial distribution model for gridding 2015 global mercury emissions. *Atmos. Environ.* **211**, 138–150 (2019).
5. UNEP, *Global Mercury Assessment 2018* (UN Environment Programme, Chemicals and Health Branch. Geneva, Switzerland, 2019).
6. H. M. Amos, D. J. Jacob, D. G. Streets, E. M. Sunderland, Legacy impacts of all-time anthropogenic emissions on the global mercury cycle. *Global Biogeochem. Cycles* **27**, 410–421 (2013).
7. Y. Zhang, *et al.*, Observed decrease in atmospheric mercury explained by global decline in anthropogenic emissions. *Proc. Natl. Acad. Sci. U.S.A.* **113**, 526–531 (2016).
8. K.-L. Chang, *et al.*, Trend detection of atmospheric time series. *Elementa: Science of the Anthropocene* **9**, 00035 (2021).
9. M. Muntean, *et al.*, Evaluating EDGARv4.tox2 speciated mercury emissions ex-post scenarios and their impacts on modelled global and regional wet deposition patterns. *Atmospheric Environment* **184**, 56–68 (2018).
10. D. G. Streets, *et al.*, Global and regional trends in mercury emissions and concentrations, 2010–2015. *Atmospheric Environment* **201**, 417–427 (2019).
11. D. Custódio, *et al.*, Odds and ends of atmospheric mercury in Europe and over the North Atlantic Ocean: temporal trends of 25 years of measurements. *Atmos. Chem. Phys.* **22**, 3827–3840 (2022).
12. K. MacSween, *et al.*, Updated trends for atmospheric mercury in the Arctic: 1995–2018. *Science of The Total Environment* **837**, 155802 (2022).
13. C. I. Olson, H. Fakhraei, C. T. Driscoll, Mercury Emissions, Atmospheric Concentrations, and Wet Deposition across the Conterminous United States: Changes over 20 Years of Monitoring. *Environ. Sci. Technol. Lett.* **7**, 376–381 (2020).
14. P. S. Weiss-Penzias, *et al.*, Trends in mercury wet deposition and mercury air concentrations across the U.S. and Canada. *Science of The Total Environment* **568**, 546–556 (2016).
15. K. Marumoto, *et al.*, Long-Term Observation of Atmospheric Speciated Mercury during 2007–2018 at Cape Hedo, Okinawa, Japan. *Atmosphere* **10**, 362 (2019).
16. L. S. P. Nguyen, G.-R. Sheu, D.-W. Lin, N.-H. Lin, Temporal changes in atmospheric mercury concentrations at a background mountain site downwind of the East Asia continent in 2006–2016. *Science of The Total Environment* **686**, 1049–1056 (2019).
17. J. Shi, *et al.*, Measurement report: Atmospheric mercury in a coastal city of Southeast China – inter-annual variations and influencing factors. *Atmos. Chem. Phys.* **22**, 11187–11202 (2022).
18. Q. Wu, *et al.*, Developing a statistical model to explain the observed decline of atmospheric mercury. *Atmospheric Environment* **243**, 117868 (2020).
19. F. Slemr, *et al.*, Atmospheric mercury in the Southern Hemisphere – Part 1: Trend and inter-annual variations in atmospheric mercury at Cape Point, South Africa, in 2007–2017, and on Amsterdam Island in 2012–2017. *Atmos. Chem. Phys.* **20**, 7683–7692 (2020).
20. M. Jiskra, *et al.*, A vegetation control on seasonal variations in global atmospheric mercury concentrations. *Nature Geosci* **11**, 244–250 (2018).
21. F. Slemr, E.-G. Brunke, R. Ebinghaus, J. Kuss, Worldwide trend of atmospheric mercury since 1995. *Atmos. Chem. Phys.* **11**, 4779–4787 (2011).
22. A. L. Soerensen, *et al.*, Multi-decadal decline of mercury in the North Atlantic atmosphere explained by changing subsurface seawater concentrations. *Geophys. Res. Lett.* **39** (2012).
23. H. Angot, *et al.*, Global and Local Impacts of Delayed Mercury Mitigation Efforts. *Environ. Sci. Technol.* **52**, 12968–12977 (2018).
24. S. N. Lyman, L. E. Gratz, S. M. Dunham-Cheatham, M. S. Gustin, A. Luippold, Improvements to the Accuracy of Atmospheric Oxidized Mercury Measurements. *Environ. Sci. Technol.* **54**, 13379–13388 (2020).
25. A. Giang, *et al.*, Understanding factors influencing the detection of mercury policies in modelled Laurentian Great Lakes wet deposition. *Environ. Sci.: Processes Impacts* **20**, 1373–1389 (2018).

26. M. Iturbide, *et al.*, An update of IPCC climate reference regions for subcontinental analysis of climate model data: definition and aggregated datasets. *Earth Syst. Sci. Data* **12**, 2959–2970 (2020).
27. Y. Tang, *et al.*, Recent decrease trend of atmospheric mercury concentrations in East China: the influence of anthropogenic emissions. *Atmos. Chem. Phys.* **18**, 8279–8291 (2018).
28. P. Sun, *et al.*, Declines of gaseous element mercury concentrations at an urban site in eastern China caused by reductions of anthropogenic emission. *Atmospheric Environment* **317**, 120199 (2024).
29. M. Muntean, *et al.*, EDGAR v8.1 Global Mercury Emissions. European Commission, Joint Research Centre (JRC) [Dataset] PID: http://data.europa.eu/89h/83b507d7-5218-4dc5-95f9-0ec36f073204. Deposited 2024.
30. H. Selin, N. E. Selin, From Stockholm to Minamata and beyond: Governing mercury pollution for a more sustainable future. *One Earth* **5**, 1109–1125 (2022).
31. D. G. Streets, *et al.*, Five hundred years of anthropogenic mercury: spatial and temporal release profiles. *Environ. Res. Lett.* **14**, 084004 (2019).
32. D. S. Stevenson, *et al.*, Trends in global tropospheric hydroxyl radical and methane lifetime since 1850 from AerChemMIP. *Atmos. Chem. Phys.* **20**, 12905–12920 (2020).
33. T. S. Dibble, H. L. Tetu, Y. Jiao, C. P. Thackray, D. J. Jacob, Modeling the OH-Initiated Oxidation of Mercury in the Global Atmosphere without Violating Physical Laws. *J. Phys. Chem. A* **124**, 444–453 (2020).
34. J. P. Parrella, *et al.*, Tropospheric bromine chemistry: implications for present and pre-industrial ozone and mercury. *Atmos. Chem. Phys.* **12**, 6723–6740 (2012).
35. A. Saiz-Lopez, *et al.*, Photochemistry of oxidized Hg(I) and Hg(II) species suggests missing mercury oxidation in the troposphere. *Proc. Natl. Acad. Sci. U.S.A.* **117**, 30949–30956 (2020).
36. X. Fu, *et al.*, Anthropogenic short-lived halogens increase human exposure to mercury contamination due to enhanced mercury oxidation over continents. *Proc. Natl. Acad. Sci. U.S.A.* **121**, e2315058121 (2024).
37. A. Cole, *et al.*, A Survey of Mercury in Air and Precipitation across Canada: Patterns and Trends. *Atmosphere* **5**, 635–668 (2014).
38. K. Schaefer, *et al.*, Potential impacts of mercury released from thawing permafrost. *Nat Commun* **11**, 4650 (2020).
39. Y. Wang, P. Wu, Y. Zhang, Climate-driven changes of global marine mercury cycles in 2100. *Proc. Natl. Acad. Sci. U.S.A.* **120**, e2202488120 (2023).
40. B. P. DiMento, R. P. Mason, S. Brooks, C. Moore, The impact of sea ice on the air-sea exchange of mercury in the Arctic Ocean. *Deep Sea Research Part I: Oceanographic Research Papers* **144**, 28–38 (2019).
41. A. Kumar, S. Wu, Y. Huang, H. Liao, J. O. Kaplan, Mercury from wildfires: Global emission inventories and sensitivity to 2000–2050 global change. *Atmospheric Environment* **173**, 6–15 (2018).
42. H. M. Horowitz, *et al.*, A new mechanism for atmospheric mercury redox chemistry: implications for the global mercury budget. *Atmos. Chem. Phys.* **17**, 6353–6371 (2017).
43. N. E. Selin, *et al.*, Chemical cycling and deposition of atmospheric mercury: Global constraints from observations. *J. Geophys. Res.* **112**, D02308 (2007).
44. Y. Zhang, *et al.*, Improved Anthropogenic Mercury Emission Inventories for China from 1980 to 2020: Toward More Accurate Effectiveness Evaluation for the Minamata Convention. *Environ. Sci. Technol.* **57**, 8660–8670 (2023).
45. Å. Iverfeldt, J. Munthe, C. Brosset, J. Pacyna, “Long-Term Changes in Concentration and Deposition of Atmospheric Mercury Over Scandinavia” in *Mercury as a Global Pollutant: Proceedings of the Third International Conference Held in Whistler, British Columbia, July 10–14, 1994*, D. B. Porcella, J. W. Huckabee, B. Wheatley, Eds. (Springer Netherlands, 1995), pp. 227–233.
46. F. Slemr, H. E. Scheel, Trends in atmospheric mercury concentrations at the summit of the Wank mountain, southern Germany. *Atmospheric Environment* **32**, 845–853 (1998).
47. K. Liu, *et al.*, Measure-Specific Effectiveness of Air Pollution Control on China’s Atmospheric Mercury Concentration and Deposition during 2013–2017. *Environ. Sci. Technol.* **53**, 8938–8946 (2019).

48. Q. Wu, *et al.*, Temporal Trend and Spatial Distribution of Speciated Atmospheric Mercury Emissions in China During 1978–2014. *Environ. Sci. Technol.* **50**, 13428–13435 (2016).
49. M. Muntean, *et al.*, Trend analysis from 1970 to 2008 and model evaluation of EDGARv4 global gridded anthropogenic mercury emissions. *Science of The Total Environment* **494–495**, 337–350 (2014).
50. H. M. Horowitz, D. J. Jacob, H. M. Amos, D. G. Streets, E. M. Sunderland, Historical Mercury Releases from Commercial Products: Global Environmental Implications. *Environ. Sci. Technol.* **48**, 10242–10250 (2014).
51. S. Y. Kwon, *et al.*, Mercury stable isotopes for monitoring the effectiveness of the Minamata Convention on Mercury. *Earth-Science Reviews* **203**, 103111 (2020).
52. J. A. Fisher, *et al.*, A synthesis of mercury research in the Southern Hemisphere, part 2: Anthropogenic perturbations. *Ambio* **52**, 918–937 (2023).
53. L. Schneider, *et al.*, A synthesis of mercury research in the Southern Hemisphere, part 1: Natural processes. *Ambio* **52**, 897–917 (2023).
54. D. S. McLagan, *et al.*, A High-Precision Passive Air Sampler for Gaseous Mercury. *Environ. Sci. Technol. Lett.* **3**, 24–29 (2016).
55. S. M. Dunham-Cheatham, S. Lyman, M. S. Gustin, Comparison and calibration of methods for ambient reactive mercury quantification. *Science of The Total Environment* **856**, 159219 (2023).
56. A. Luippold, *et al.*, Use of Multiple Lines of Evidence to Understand Reactive Mercury Concentrations and Chemistry in Hawai'i, Nevada, Maryland, and Utah, USA. *Environ. Sci. Technol.* **54**, 7922–7931 (2020).
57. F. De Simone, *et al.*, A Chemical Transport Model Emulator for the Interactive Evaluation of Mercury Emission Reduction Scenarios. *Atmosphere* **11**, 878 (2020).
58. C. W. Tessum, J. D. Hill, J. D. Marshall, InMAP: A model for air pollution interventions. *PLoS ONE* **12**, e0176131 (2017).
59. W. Atkinson, *et al.*, A tool for air pollution scenarios (TAPS v1.0) to enable global, long-term, and flexible study of climate and air quality policies. *Geosci. Model Dev.* **15**, 7767–7789 (2022).
60. A. Dastoor, *et al.*, The Multi-Compartment Hg Modeling and Analysis Project (MCHgMAP): Mercury modeling to support international environmental policy. *Geoscientific Model Development Discussions* **2024**, 1–171 (2024).
61. P. J. Blanchfield, *et al.*, Experimental evidence for recovery of mercury-contaminated fish populations. *Nature* **601**, 74–78 (2022).
62. A. Steffen, *et al.*, A synthesis of atmospheric mercury depletion event chemistry in the atmosphere and snow. *Atmospheric Chemistry and Physics* **8**, 1445–1482 (2008).
63. M. S. Gustin, *et al.*, Do We Understand What the Mercury Speciation Instruments Are Actually Measuring? Results of RAMIX. *Environ. Sci. Technol.* **47**, 7295–7306 (2013).
64. D. A. Gay, *et al.*, The Atmospheric Mercury Network: measurement and initial examination of an ongoing atmospheric mercury record across North America. *Atmos. Chem. Phys.* **13**, 11339–11349 (2013).
65. K. Tørseth, *et al.*, Introduction to the European Monitoring and Evaluation Programme (EMEP) and observed atmospheric composition change during 1972–2009. *Atmos. Chem. Phys.* **12**, 5447–5481 (2012).
66. F. Sprovieri, *et al.*, Atmospheric mercury concentrations observed at ground-based monitoring sites globally distributed in the framework of the GMOS network. *Atmos. Chem. Phys.* **16**, 11915–11935 (2016).
67. V. L. St. Louis, *et al.*, Atmospheric Concentrations and Wet/Dry Loadings of Mercury at the Remote Experimental Lakes Area, Northwestern Ontario, Canada. *Environ. Sci. Technol.* **53**, 8017–8026 (2019).
68. F. Carbone, *et al.*, Sea surface temperature variation linked to elemental mercury concentrations measured on Mauna Loa. *Geophys. Res. Lett.* **43**, 7751–7757 (2016).
69. M. S. Landis, R. K. Stevens, F. Schaedlich, E. M. Prestbo, Development and Characterization of an Annular Denuder Methodology for the Measurement of Divalent Inorganic Reactive Gaseous Mercury in Ambient Air. *Environ. Sci. Technol.* **36**, 3000–3009 (2002).
70. S. Sholupov, S. Pogarev, V. Ryzhov, N. Mashyanov, A. Stroganov, Zeeman atomic absorption spectrometer RA-915+ for direct determination of mercury in air and complex matrix samples. *Fuel Processing Technology* **85**, 473–485 (2004).

71. Å. Iverfeldt, Occurrence and turnover of atmospheric mercury over the nordic countries. *Water, Air, and Soil Pollution* **56**, 251–265 (1991).
72. K.-L. Chang, M. G. Schultz, G. Koren, Selke, Niklas, Guidance note on best statistical practices for TOAR analyses. Available at: https://doi.org/10.48550/arXiv.2304.14236. (2023).
73. D. Bates, M. Mächler, B. Bolker, S. Walker, Fitting Linear Mixed-Effects Models Using **lme4**. *J. Stat. Soft.* **67** (2015).
74. R. Koenker, K. F. Hallock, Quantile Regression. *The Journal of Economic Perspectives* **15**, 143–156 (2001).
75. K.-L. Chang, *et al.*, Impact of the COVID-19 Economic Downturn on Tropospheric Ozone Trends: An Uncertainty Weighted Data Synthesis for Quantifying Regional Anomalies Above Western North America and Europe. *AGU Advances* **3**, e2021AV000542 (2022).
76. W. C. Porter, C. L. Heald, D. Cooley, B. Russell, Investigating the observed sensitivities of air-quality extremes to meteorological drivers via quantile regression. *Atmos. Chem. Phys.* **15**, 10349–10366 (2015).
77. R. Koenker, quantreg: Quantile Regression. Available at: https://CRAN.R-project.org/package=quantreg. (2022).
78. A. Feinberg, T. Dlamini, M. Jiskra, V. Shah, N. E. Selin, Evaluating atmospheric mercury (Hg) uptake by vegetation in a chemistry-transport model. *Environ. Sci.: Processes Impacts* **24**, 1303–1318 (2022).
79. M. D. McKay, R. J. Beckman, W. J. Conover, Comparison of Three Methods for Selecting Values of Input Variables in the Analysis of Output from a Computer Code. *Technometrics* **21**, 239–245 (1979).
80. N. E. Selin, A proposed global metric to aid mercury pollution policy. *Science* **360**, 607–609 (2018).
81. H. M. Amos, *et al.*, Global Biogeochemical Implications of Mercury Discharges from Rivers and Sediment Burial. *Environ. Sci. Technol.* **48**, 9514–9522 (2014).
82. R. Gelaro, *et al.*, The Modern-Era Retrospective Analysis for Research and Applications, Version 2 (MERRA-2). *J. Clim.* **30**, 5419–5454 (2017).
83. P. D. Nightingale, *et al.*, In situ evaluation of air-sea gas exchange parameterizations using novel conservative and volatile tracers. *Global Biogeochem. Cycles* **14**, 373–387 (2000).
84. S. Song, *et al.*, Top-down constraints on atmospheric mercury emissions and implications for global biogeochemical cycling. *Atmos. Chem. Phys.* **15**, 7103–7125 (2015).
85. N. E. Selin, *et al.*, Global 3-D land-ocean-atmosphere model for mercury: Present-day versus preindustrial cycles and anthropogenic enrichment factors for deposition. *Global Biogeochem. Cycles* **22**, GB2011 (2008).
86. G. R. van der Werf, *et al.*, Global fire emissions estimates during 1997–2016. *Earth Syst. Sci. Data* **9**, 697–720 (2017).

Figures

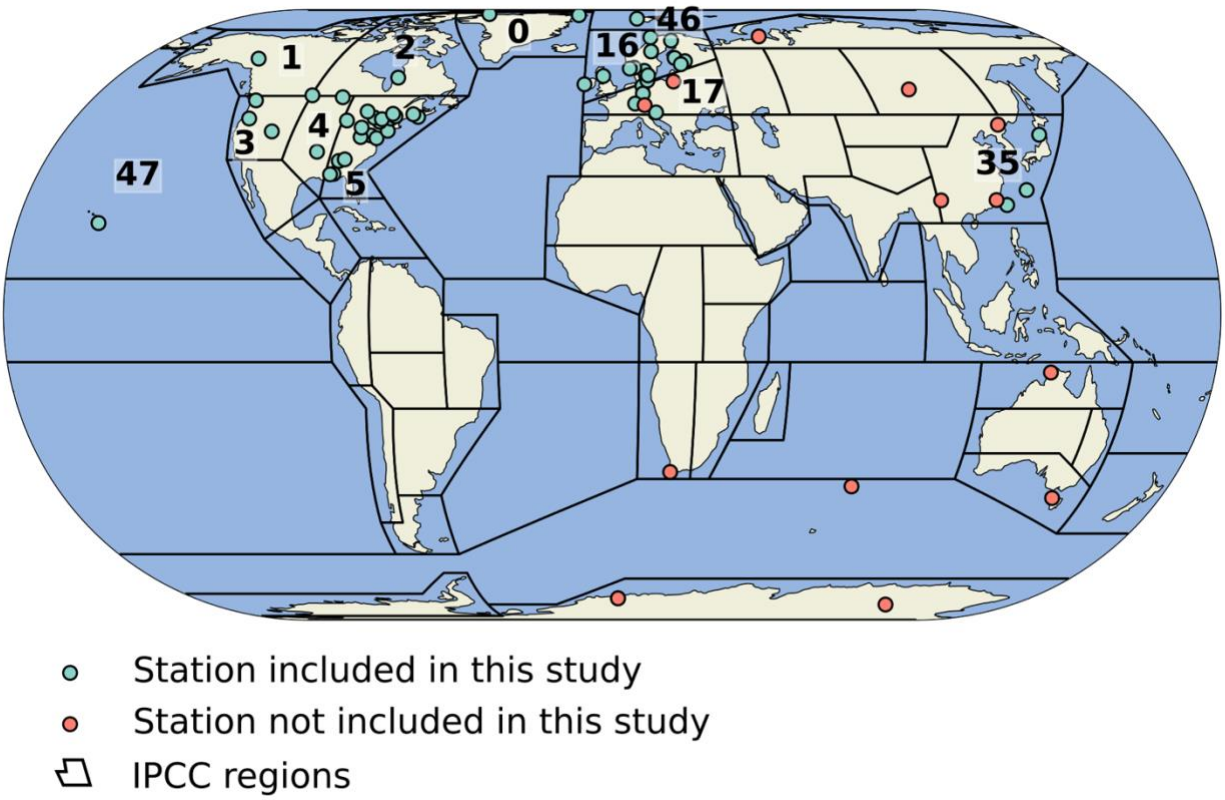

Figure 1. Map of observation stations that measured atmospheric Hg concentrations for more than 6 years (Table S1). Defined regions (26) are indicated with black lines, with corresponding numbering of included regions listed on the map. For this study, we included NH stations with openly accessible or provided datasets.

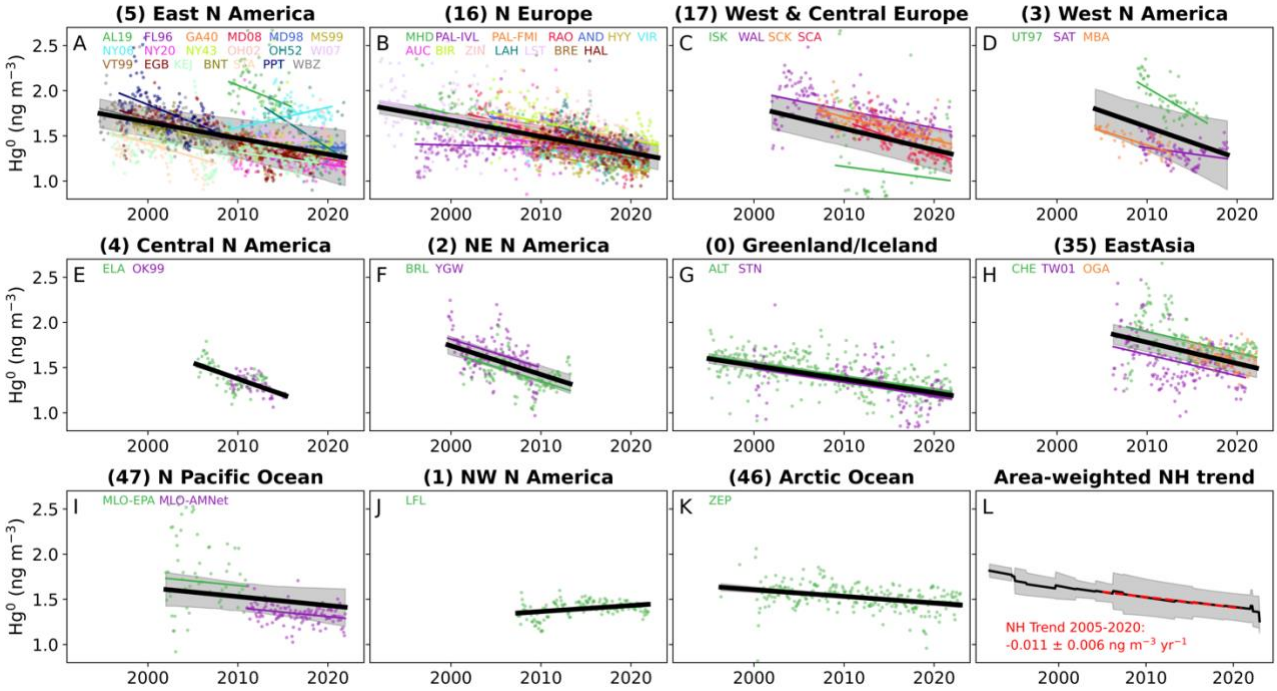

Figure 2. Trends in observed gaseous elemental mercury (Hg^0) aggregated by the regions (*A*–*K*) in Fig. 1 (labelled by region number). Trends are calculated with linear mixed effects modeling, with overall regional trends shown in black and shading shows the 5th to 95th percentile range. Individual site deseasonalized monthly means are shown as colored points and individual regressions as colored lines. The overall Northern Hemisphere (NH) trend (*L*) is calculated by taking the area-weighted average of regional trends, with the shading showing the 2σ averaging error. The red dashed curve in *L* is the linear regression trend for 2005–2020, with trend error representing 2σ error from resampling regional trends within their error bounds. We distinguished data from sites where measurements were made by multiple networks, i.e., Pallas (FMI and IVL) and Mauna Loa (EPA and AMNet).

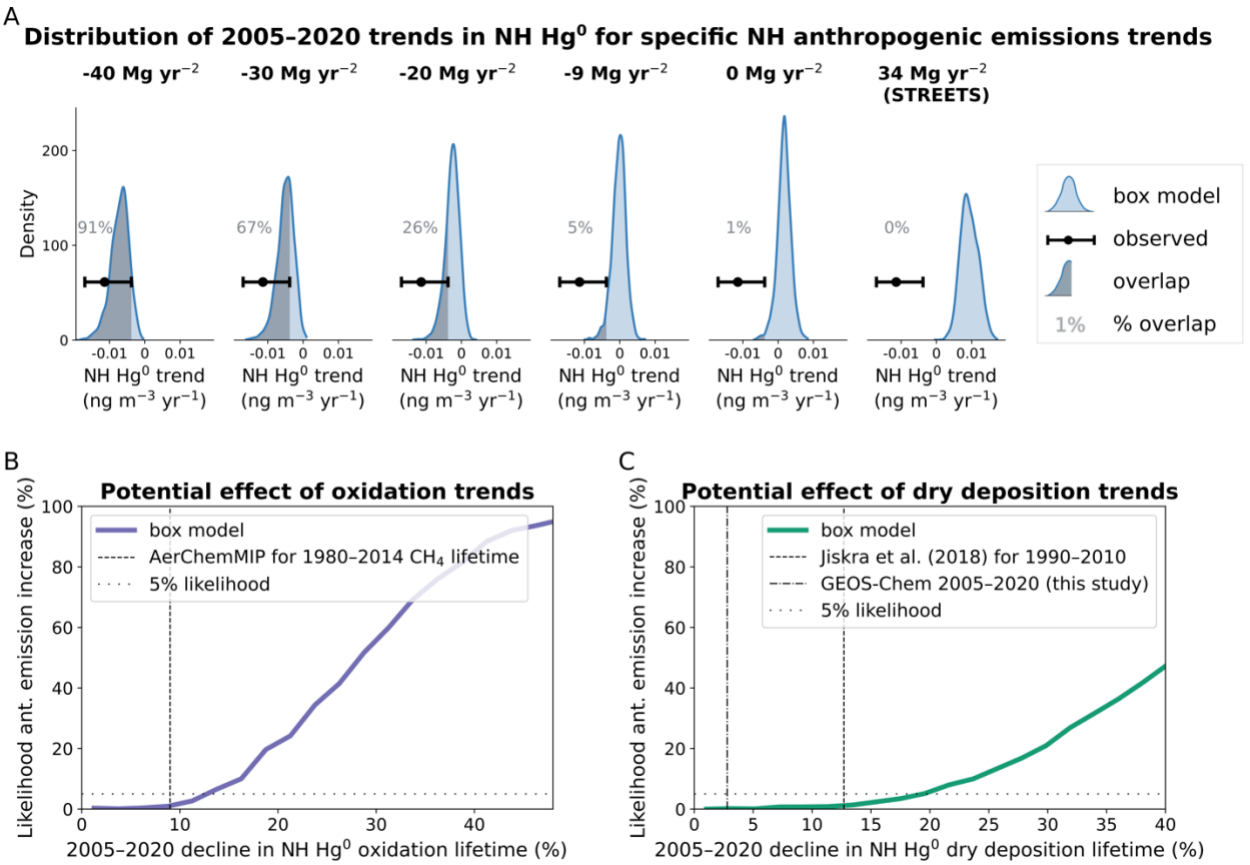

Figure 3. Modeled relationships between 2005–2020 trends in NH Hg^0 concentrations and drivers. (*A*) Histograms showing relationship between 2005–2020 trends in anthropogenic NH emissions and NH Hg^0 trends. We select scenarios with different anthropogenic emissions trend values from the 10^5 box model simulations (with a window of ±1 Mg yr^{-2} to yield ~2000 simulations for each trend value). Blue histograms illustrate the probability density of simulated NH Hg^0 trends for each emission trend value. Observed NH Hg^0 trends are shown in the horizontal black line with error bars. The shaded overlap represents the area of the histogram where the model is compatible with observed trends, with the percent of total area shown in grey. The histogram for the anthropogenic emissions trend of 34 Mg yr^{-2} represents the Streets et al. (10) 2005–2015 trend. (*B*) Impact of NH Hg^0 oxidation lifetime trends on the likelihood of positive anthropogenic (ant.) trends for 2005–2020. The x-axis shows the relative decline (%) in the NH Hg^0 oxidation lifetime between 2005 and 2020. The y-axis refers to the percent of box model runs fitting with the observed NH Hg^0 trend (± 2σ) that have positive anthropogenic emissions trends. The AerChemMIP (32) estimate for the relative change 1980-2014 methane (CH_4) oxidation lifetime is shown for context. (*C*) Impact of NH Hg^0 dry deposition lifetime on the likelihood of positive anthropogenic (ant.) trends for 2005–2020. The x-axis shows the relative decline (%) in the NH Hg^0 dry deposition lifetime between 2005 and 2020. The estimated trend in NH dry deposition from Jiskra et al. (20) for 1990–2010 is shown for context, as well as the GEOS-Chem simulated 2005–2020 trend (Fig. S10).

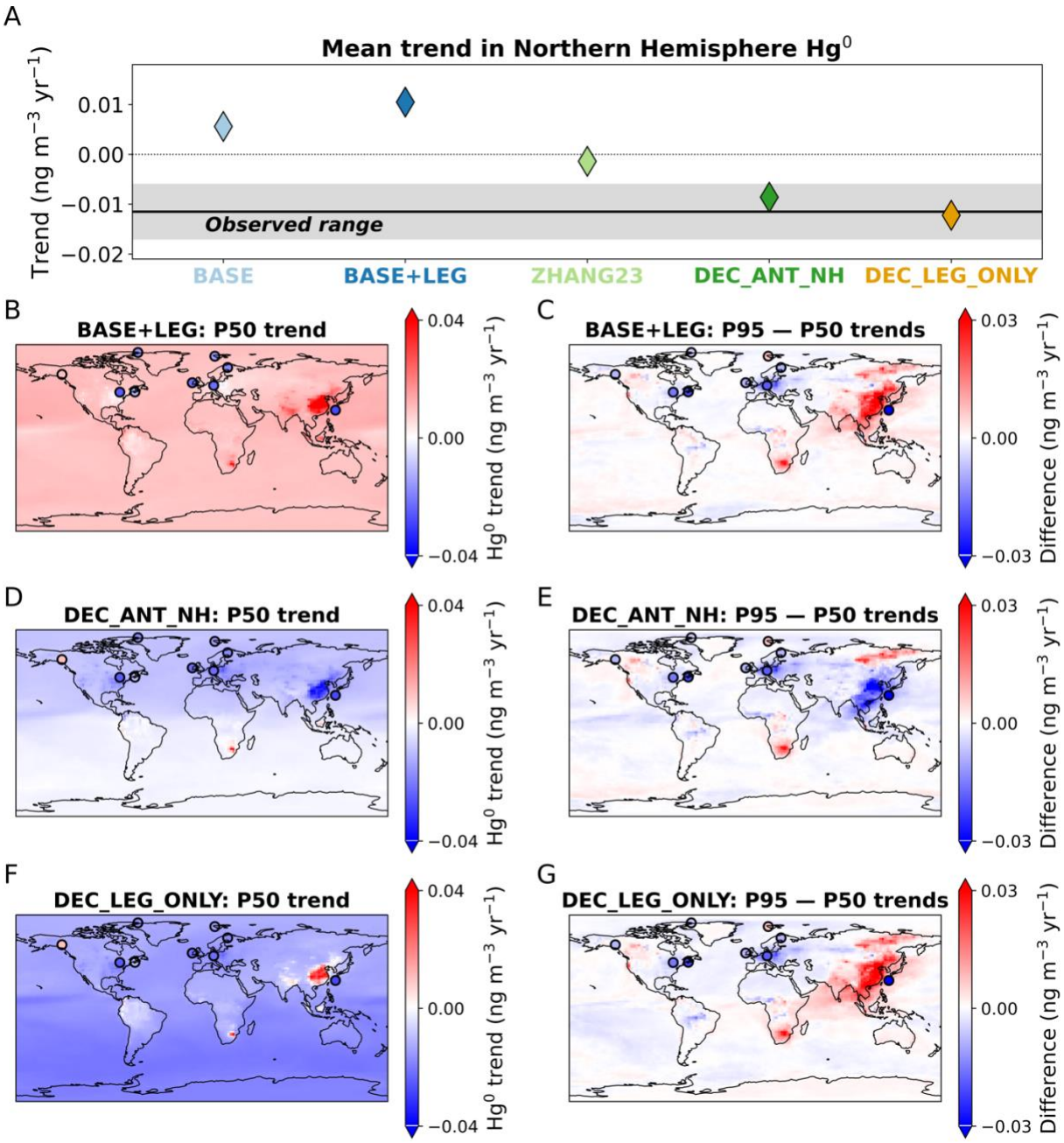

Figure 4. Comparison between trends (2005–2020) in GEOS-Chem model simulations and observations for Northern Hemisphere (NH) mean Hg^0 (*A*), calculated using linear mixed effects modeling of available NH regions and calculating the area-weighted mean (Fig. 2). The observed range in the NH Hg^0 trend is shown as a black line (mean) with shaded area (±2σ). Error bars are smaller than the markers for the model simulations. Trend in median (P50) daily deseasonalized simulated values in BASE+LEG (*B*), DEC_ANT_NH (*D*), and DEC_LEG_ONLY (*F*) for each model grid cell. BASE+LEG is the simulation with Streets et al. (10) emissions and associated legacy feedbacks, DEC_ANT_NH is the simulation with decreasing anthropogenic emissions in the NH, and DEC_LEG_ONLY includes a decline in legacy emissions from the ocean (Table 1). Observed results are plotted in filled circles for 9 stations with more than 13 years of high frequency data. Differences between 95th percentile (P95) trend and median (P50) trend shown for BASE+LEG (*C*), DEC_ANT_NH (*E*), and DEC_LEG_ONLY (*G*) simulations and observations. The other simulations are shown in Fig. S12.

843 **Table 1**. Description of Hg simulations conducted in GEOS-Chem for 2005–2020.

Simulation	Anthropogenic emissions	Legacy re-emissions	Anthropogenic NH emissions trend (Mg yr^{-2})	Overall NH emissions trend (Mg yr^{-2})
BASE	2005–2015: Streets et al. (10) 2016–2020: repeat 2015	Constant interannually; based on Horowitz et al. (42)	+23	+18
BASE+LEG	2005–2015: Streets et al. (10) 2016–2020: repeat 2015	Trend from median response to BASE anthropogenic emissions trend (Fig. S8F)	+23	+31
ZHANG23	2005–2020 Chinese emissions from BASE are scaled by emission inventory trend from Zhang et al. (44)	Trend from median response to ZHANG23 anthropogenic emissions trend (Fig. S8F)	–11	–12
DEC_ANT_NH	ZHANG23 emissions with additional 23 Mg yr^{-2} decrease in anthropogenic emissions spread across NH outside China	Trend from median response to DEC_ANT_NH anthropogenic emissions trend (Fig. S8F)	–34	–41
DEC_LEG_ONLY	2005–2015: Streets et al. (10) 2016–2020: repeat 2015	Decline imposed	+23	–30

844

Supplementary Information (SI) for

Unexpected anthropogenic emission decreases are required to explain recent atmospheric mercury concentration declines

Aryeh Feinberg[a]*, Noelle E. Selin[a,b], Christine F. Braban[c], Kai-Lan Chang[d,e], Danilo Custódio[f], Daniel A. Jaffe[g,h], Katriina Kyllönen[i], Matthew S. Landis[j], Sarah R. Leeson[c], Winston Luke[k], Koketso M. Molepo[l], Marijana Murovec[m], Michelle G. Nerentorp Mastromonaco[n], Katrine Aspmo Pfaffhuber[o], Julian Rüdiger[p], Guey-Rong Sheu[q], and Vincent L. St.Louis[r]

[a] *Institute for Data, Systems, and Society, Massachusetts Institute of Technology, Cambridge, MA 02139, USA*

[b] *Department of Earth, Atmospheric, and Planetary Sciences, Massachusetts Institute of Technology, Cambridge, MA 02139, USA*

[c] *UK Centre for Ecology & Hydrology (UKCEH), Penicuik, Midlothian EH26 0QB, UK*

[d] *Cooperative Institute for Research in Environmental Sciences, University of Colorado, Boulder, CO 80309-0401, USA*

[e] *NOAA Chemical Sciences Laboratory, Boulder, CO 80305, USA*

[f] *Max-Planck-Institut für Biogeochemie, D-07745 Jena, Germany*

[g] *School of STEM, University of Washington Bothell, Bothell, WA 98011, USA*

[h] *Department of Atmospheric Sciences, University of Washington Seattle, Seattle, WA 98195, USA*

[i] *Finnish Meteorological Institute, Helsinki 00560, Finland*

[j] *United States Environmental Protection Agency, Office of Research and Development, Research Triangle Park, NC 27711, USA*

[k] *NOAA/Air Resources Laboratory, College Park, MD 20740, USA*

[l] *Institute of Coastal Environmental Chemistry, Helmholtz Zentrum Hereon, 21502 Geesthacht, Germany*

[m] *Slovenian Environment Agency, Environment and Nature protection Office, Air Quality Division,1000 Ljubljana, Slovenia*

[n] *IVL Swedish Environmental Research Institute, SE-411 33 Gothenburg, Sweden*

[o] *NILU, 2027 Kjeller, Norway*

[p] *Air Monitoring Network, German Environment Agency, 63225 Langen, Germany*

[q] *Department of Atmospheric Sciences, National Central University, Taoyuan 320, Taiwan*

[r] *Department of Biological Sciences, University of Alberta, Edmonton, AB T6G 2E9, Canada*

*Correspondence to: arifeinberg@gmail.com (A.F.)

This PDF file includes:

Section S1. Observation station information

Table S1. List of sites measuring gaseous elemental mercury (GEM: Hg^0) included in this study.

Site code	Location	Latitude	Longitude	Measurement Network	IPCC Region[a]	Years available
AL19	Birmingham, USA	33.6	-86.8	AMNet[b]	5	2009–2015
FL96	Pensacola, USA	30.5	-87.4	AMNet[b]	5	2009–2015
GA40	Yorkville, USA	33.9	-85.0	AMNet[b]	5	2009–2015
MD08	Piney Reservoir, USA	39.7	-79.0	AMNet[b]	5	2009–2021
MD98	Beltsville, USA	39.0	-76.8	AMNet[b]	5	2009–2021
MS99	Grand Bay, USA	30.4	-88.4	AMNet[b]	5	2009–2020
NY06	Bronx, USA	40.9	-73.9	AMNet[b]	5	2008–2020
NY20	Huntington Forest, USA	44.0	-74.2	AMNet[b]	5	2009–2021
NY43	Rochester, USA	43.1	-77.5	AMNet[b]	5	2008–2020
OH02	Athens, USA	39.3	-82.1	AMNet[b]	5	2009–2020
OH52	South Bass Island, USA	41.7	-82.8	AMNet[b]	5	2013–2021
OK99	Stilwell, USA	35.8	-94.7	AMNet[b]	4	2009–2015
UT97	Salt Lake City, USA	40.7	-112.0	AMNet[b]	3	2008–2017
VT99	Underhill, USA	44.5	-72.9	AMNet[b]	5	2009–2016
WI07	Horicon Marsh, USA	43.5	-88.6	AMNet[b]	5	2011–2017
MLO	Mauna Loa, USA	19.5	-155.6	AMNet[b]/EPA[c]/NOAA	47	2002–2021
MBA	Mt. Bachelor, USA	44.0	-121.7	GMOS[d]	3	2004–2012
ALT	Alert, Canada	82.5	-62.3	CAPMoN[e]	0	1995–2021
BNT	Burnt Island, Canada	45.8	-82.9	CAPMoN[e]	5	1998–2007
BRL	Bratt's Lake, Canada	50.2	-104.7	CAPMoN[e]	2	2001–2013
EGB	Egbert, Canada	44.2	-79.8	CAPMoN[e]	5	1996–2018
KEJ	Kejimkujik, Canada	44.4	-65.2	AMNet[b]/CAPMoN[e]	5	1996–2018
LFL	Little Fox Lake, Canada	61.4	-135.6	CAPMoN[e]	1	2007–2021
PPT	Point Petre, Canada	43.8	-77.1	CAPMoN[e]	5	1996–2007
SAT	Saturna, Canada	48.8	-123.2	CAPMoN[e]	3	2009–2018
STA	Huntsman Science Centre, Canada	45.1	-67.1	CAPMoN[e]	5	1995–2007
WBZ	St. Anicet, Canada	45.1	-74.3	CAPMoN[e]	5	1994–2009
YGW	Kuujuarapik, Canada	55.3	-77.7	CAPMoN[e]	2	1999–2009
ELA	Experimental Lakes Area, Canada	49.7	-93.7	IISD[f]	4	2005–2013
AND	Andøya, Norway	69.3	16.0	EMEP[g]	16	2004–2021
AUC	Auchencorth Moss, UK	55.8	-3.2	EMEP[g]	16	2006–2022
BIR	Birkenes, Norway	58.4	8.3	EMEP[g]	16	2004–2023
BRE	Bredkälen, Sweden	63.9	15.3	EMEP[g]	16	2009–2021
HAL	Hallahus/Vavihill[h], Sweden	56.0	13.1	EMEP[g]	16	2009–2021
HYY	Hyytiälä, Finland	61.6	24.0	EMEP[g]	16	2009–2021
ISK	Iskrba, Slovenia	45.6	14.9	EMEP[g]	17	2009–2021
LAH	Lahemaa, Estonia	59.5	25.9	EMEP[g]	16	2012–2021
LST	Lista, Norway	58.1	6.6	EMEP[g]	16	1992–2004
MHD	Mace Head, Ireland	53.3	-9.9	EMEP[g]/GMOS[d]	16	1996–2022
PAL	Pallas, Finland	68.0	24.4	EMEP[g]/GMOS[d]	16	1996–2021
RAO	Råö, Sweden	57.4	11.9	EMEP[g]/GMOS[d]	16	2002–2020
SCA	Schauinsland, Germany	47.9	7.9	EMEP[g]	17	2011–2021
SCK	Schmücke, Germany	50.7	10.8	EMEP[g]	17	2007–2021
STN	Station Nord/Villum, Greenland	81.6	-16.6	EMEP[g]	0	2000–2021
VIR	Virolahti, Finland	60.5	27.7	EMEP[g]	16	2008–2021
WAL	Waldhof, Germany	52.8	10.8	EMEP[g]	17	2002–2021
ZEP	Zeppelin, Norway	78.9	11.9	EMEP[g]	46	1996–2022
ZIN	Zingst, Germany	54.4	12.7	EMEP[g]	16	1999–2021
TW01	Mt. Lulin, Taiwan	23.5	120.9	AMNet[b] / MOENV Taiwan[i]	35	2006–2020
CHE	Cape Hedo, Japan	26.9	128.3	MOEJ[j]	35	2007–2022
OGA	Oga Peninsula, Japan	39.9	139.9	MOEJ[j]	35	2014–2022

[a] IPCC regions are defined with the numbering in Fig. 1, taken from Iturbide et al. (1) [b] Gay et al. (2)
[c] Carbone et al. (3) [d] Sprovieri et al. (4) [e] Cole et al. (5) [f] St. Louis et al. (6) [g] Tørseth et al. (7)
[h] Site changed location in 2016, but due to nearby locations (<3 km apart), they are combined in this analysis
[i] Nguyen et al. (8) [j] Marumoto et al. (9)

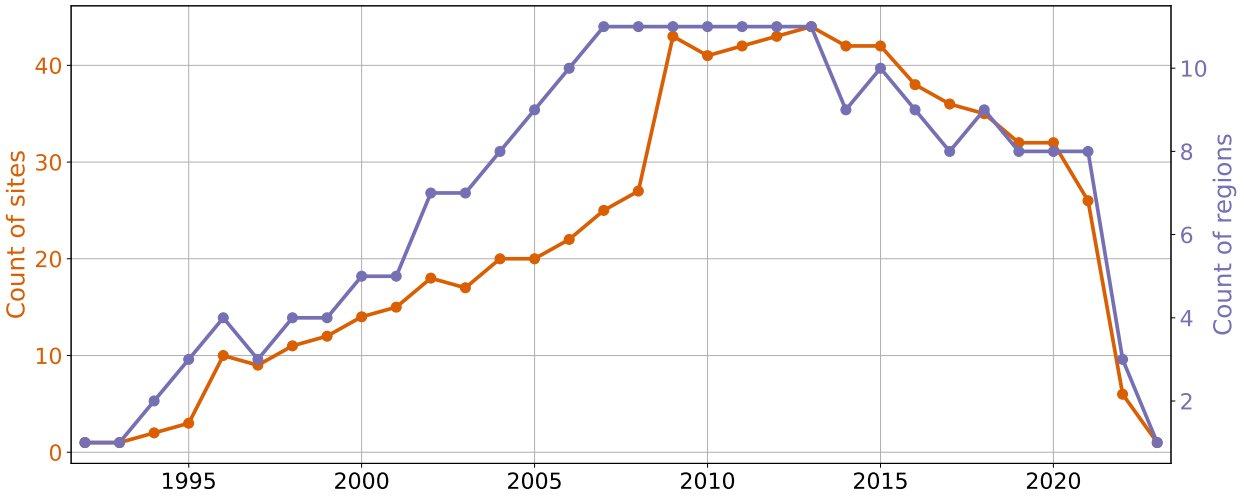

Figure S1. Timeseries showing count of measurement sites included in this study by operation year. The orange curve shows the number of sites measured in each year and the purple curve shows the number of Northern Hemisphere (NH) IPCC regions (Fig. 1) measured in each year. Note that 2022 and 2023 data may still be undergoing quality control procedures by networks and therefore was not yet released at the time of analysis; more data from these years will likely be made available in the future.

Section S2. Trend results by region

Table S2. Tabulated overall regional trends (± 2σ) calculated through linear mixed effects modelling for full available time period of each region.

Region name (number)	Number of sites	Area (10^6 km^2)	Trend (ng m^{-3} yr^{-1})	Time period
Eastern North America (5)	19	5.69	-0.016 ± 0.011	1994–2022
Northern Europe (16)	13	5.00	-0.018 ± 0.004	1992–2023
West & Central Europe (17)	4	3.79	-0.024 ± 0.010	2002–2021
Western North America (3)	3	3.14	-0.035 ± 0.025	2004–2018
Central North America (4)	2	2.93	-0.035 ± 0.007	2005–2015
Northeastern North America (2)	2	7.66	-0.032 ± 0.009	1999–2013
Greenland/Iceland (0)	2	4.77	-0.015 ± 0.003	1995–2021
East Asia (35)	3	9.46	-0.023 ± 0.005	2006–2022
North Pacific Ocean (47)	1	51.61	-0.010 ± 0.011	2002–2021
Northwestern North America (1)	1	7.51	0.007 ± 0.003	2007–2021
Arctic Ocean (1)	1	6.35	-0.007 ± 0.002	1996–2022
Northern Hemisphere (NH) area-weighted average	**51**		**-0.011 ± 0.006**	**2005–2020**

Section S3. Sensitivity of trends to statistical approach

Section S3.1 Modelled differences between site, surface, and troposphere NH trends

We used the five GEOS-Chem simulations to test different approaches for calculating overall trends in NH Hg^0 (Fig. S2). We calculated annual averages of the model results over the entire NH troposphere (orange lines), representative of the NH tropospheric box in the 3-box model simulations. We compared this to simulated NH surface Hg^0 concentrations (purple lines), which is the quantity that can actually be measured by surface observation stations. The calculated 2005–2020 trends in surface Hg^0 agree within 0.0007 ng m^{-3} yr^{-1} of tropospheric Hg^0 trends for all simulations except DEC_ANT_NH, where surface declines are faster than tropospheric declines by 0.0015 ng m^{-3} yr^{-1}. This can be explained by enhanced dilution of the negative emissions trends when considering the whole troposphere versus the surface level. To approximate the real situation where only a small fraction of the NH surface is measured, we averaged only the model grid cells that contain the 51 observation sites (magenta line in Fig. S2). This approach leads to biases of up to 0.0044 ng m^{-3} yr^{-1} due to the uneven distribution of observation stations (Fig. 1) throughout the NH, with some regions covered more than others and other regions having no observations. This bias can be reduced to below 0.0006 ng m^{-3} yr^{-1} by first averaging by IPCC region the grid cells that correspond to observation sites (Fig. 1) and then calculating an area-weighted average for the NH (green line), similar to what was done for the observation analysis in the main manuscript (Fig. 2). Therefore, it is best to use the approach of area-weighted site averages when limited observation stations are available, leading to good agreement with the surface trends in Hg^0. We expanded the observed trend uncertainty in Figs. 3A and B upwards by 0.0021 ng m^{-3} yr^{-1} (max error between area-weighted and tropospheric trends, DEC_ANT_NH), due to the potential overestimate of NH tropospheric trends by only having surface observations (Fig. S2).

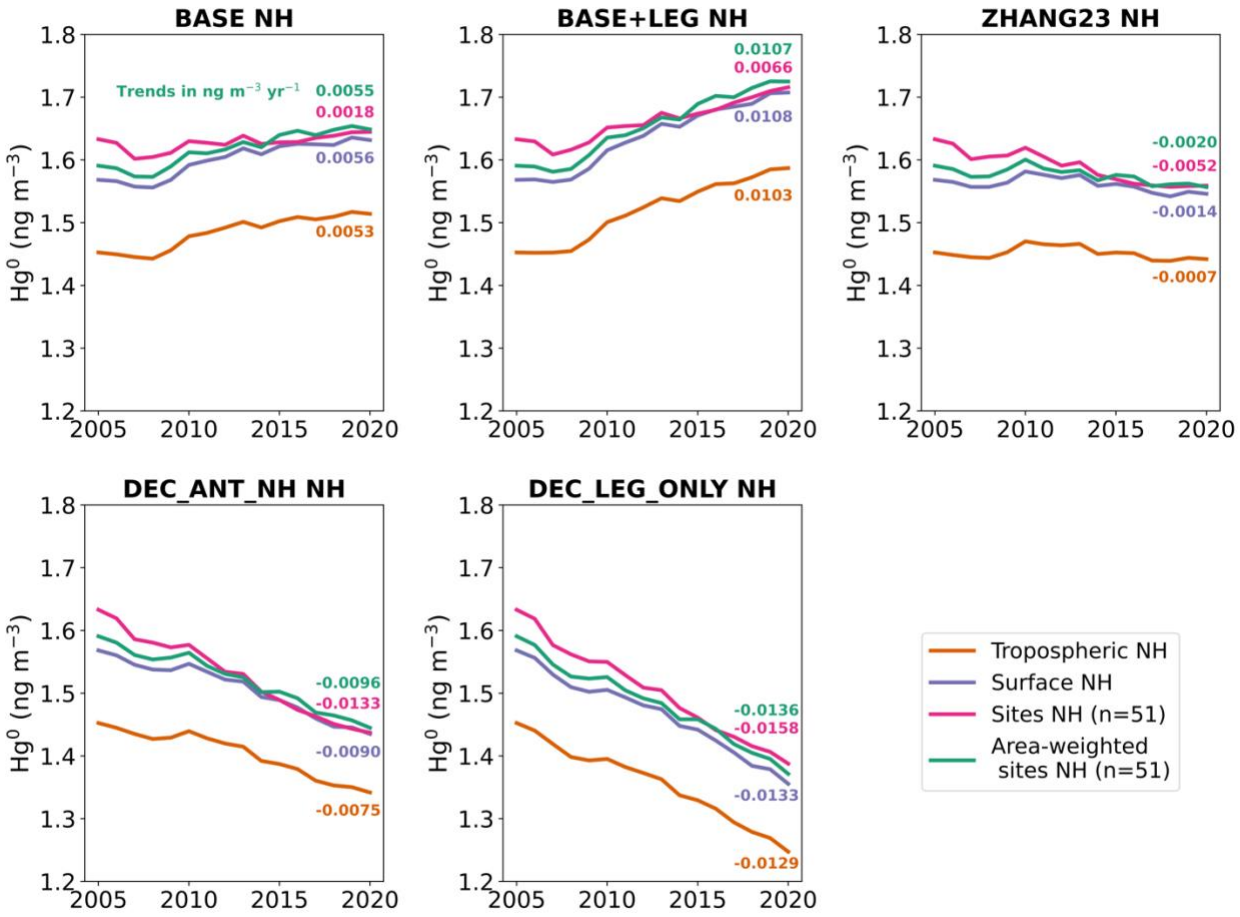

Figure S2. Different methods of calculating hemispheric average trends applied to GEOS-Chem simulated Hg^0. We compared annual mean simulated timeseries of: 1) NH tropospheric averages, 2) NH surface averages, 3) averaging model grid cells where observation sites are located, and 4) area-weighted averaging of regional averages of model grid cells where observation sites are located. Linear regression trends over 2005–2020 are listed in units of ng m^{-3} yr^{-1}.

Section S3.2 Aggregation of observation stations into overall NH annual averages using "bucket" method

Previous studies (e.g., 10) have calculated overall timeseries for regions by averaging all available stations for each specific year ("bucket" method). Biases can arise in this approach from multiple sources of error: 1) sites have individual offsets and trends due to measurement method differences or specific local sources, leading to biases in a "bucket" average because sites do not all cover the same time period; 2) sites are unevenly distributed, with certain regions over- or under-represented; and 3) certain months can be missing in a specific year, which due to the strong seasonality of Hg^0 can bias the annual mean. We aimed to address the drawbacks of the "bucket" approach by explicitly modeling offsets between sites using linear mixed effects models, deseasonalizing monthly means from all observations, and aggregating results by IPCC regions before calculating area-weighted averages. To compare our methods with approaches applied in previous papers, we use the bucket approach to calculate 2005–2020 trends in Eastern North America (19 sites), Northern Europe (13 sites), and the NH (51 sites) (Fig. S3) in a sensitivity test. Overall, the derived trends are similar for the NH between our approach (-0.011 ± 0.006 ng m^{-3} yr^{-1}) and the "bucket" approach (-0.015 ng m^{-3} yr^{-1}). Issues with the bucket method were observed for periods when less sites are available (e.g., before the year 2000 in Fig. S3), which show high variability due to differences in the number and characteristics of averaged sites for each year.

Therefore, we recommend that caution be exercised with such an approach, as the derived aggregated timeseries may be misleading and could be misinterpreted as real variability rather than changes in site availability.

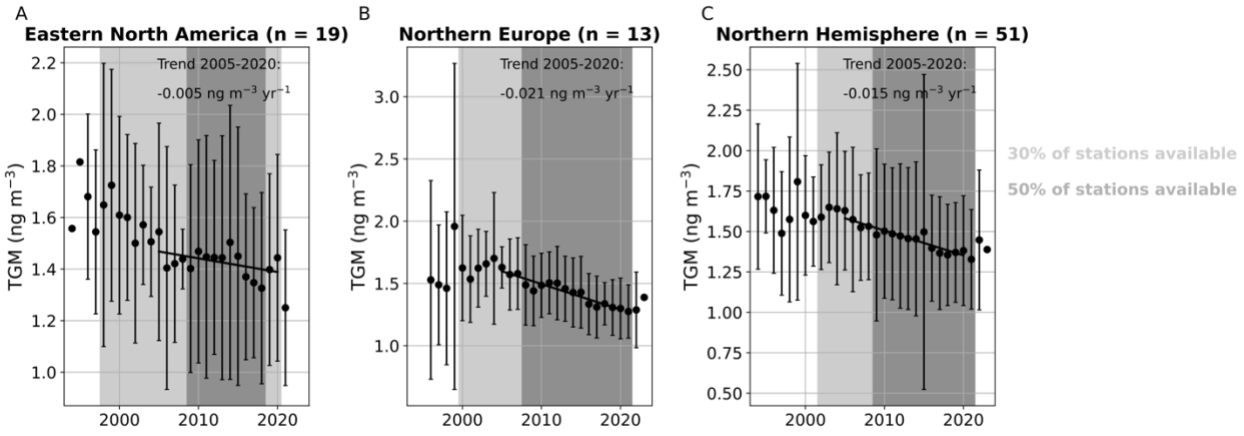

Figure S3. "Bucket" method trends calculated by averaging all available station data (not deseasonalized) for each year for Eastern North America (*A*), Northern Europe (*B*), and the overall Northern Hemisphere (*C*). Error bars show the 2σ variation in station averages. Shading shows the years where at least 30% (light gray) and 50% of the stations (dark gray) are available. Linear regression trends are calculated over 2005–2020 and listed on the plot.

Section S3.3 Using Generalized Additive Models (GAM) to aggregate multisite data

To test the robustness of our regional trend results to other approaches, we applied the approach of Chang et al. (11) to use Generalized Additive Models (GAM) to aggregate multisite data into an overall trend. In this regression-based approach, we modeled the deseasonalized Hg^0 monthly mean values at multiple sites as a function of site (s) and time (t):

$$\text{obs}(s,t) = \text{regional trend}(t) + \text{regional seasonality}(t) + \text{site offset}(s) + \text{site-specific trend}(s,t) + \text{site-specific seasonality}(s,t) + \text{AR}(1)\ \text{error} \quad \text{(Eq. S1)}$$

The GAM approach fits smooth functions of the predictor variables, which include time, month-of-year (for seasonality), and the categorical site ID (for site-specific terms). We used the implementation of GAM in the R package mgcv (12) and calculated fits using the restricted maximum likelihood (REML) method to avoid overfitting.

The GAM method is not suitable when only a few sites are available within a region (13), so in the main manuscript we focused on linear mixed effect models of regional trends. For the GAM analysis here, we investigated the two regions with more than 10 sites (Eastern North America and Northern Europe). GAM helped to identify nonlinearities in the overall regional trend, for example, a deceleration in the Eastern North America Hg^0 decline occurred after ~2009. A previous study has suggested a deceleration in Hg^0 trends in North America around 2008, although different statistical methods were applied on a smaller set of stations (14). We calculated the 2005–2020 linear trend obtained from the GAM curves for Eastern North America (-0.011 ng m^{-3} yr^{-1}) and Northern Europe (-0.019 ng m^{-3} yr^{-1}). Since both of these trends are within the error of the results obtained for linear mixed effects modeling (Eastern North America: -0.016 ± 0.011 ng m^{-3} yr^{-1}; Northern Europe: -0.018 ± 0.004 ng m^{-3} yr^{-1}), we conclude that the derived regional declines are relatively robust to the choice of statistical approach.

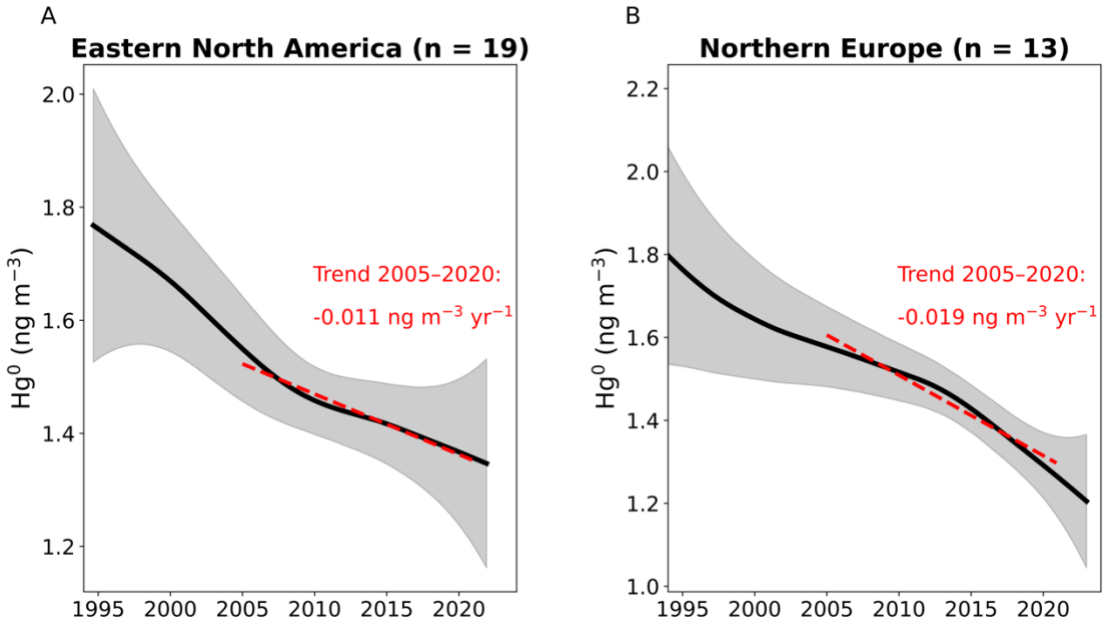

Figure S4. Generalized additive model (GAM) regional trends for multisite deseasonalized total gaseous mercury (Hg^0) data in Eastern North America (*A*) and Northern Europe (*B*). The GAM mean estimate is shown as a black line, with shaded grey areas showing ± 2 standard errors in the GAM estimate. Linear regression trends (red dashed lines) were calculated over the 2005–2020 period from the regional nonlinear GAM curve.

Section S3.4 Restricting the analysis to site data between 2005 and 2020

In the main manuscript (Fig. 2), we use the full set of available data between 1992 and 2022 to calculate linear mixed effects model trends for each region, which are then area-weighted to calculate an average 2005–2020 trend for the Northern Hemisphere (NH). We use the full extent of data to maximize the available information in the calculation of long-term Hg^0 trends. Here, we repeat the analysis but only use data between 2005 and 2020 to calculate the trend, removing all earlier and later data from the analysis. The results are summarized in Fig. S5 and Table S3, which can be compared to Fig. 2 and Table S2. Overall, the regional trends calculated with both datasets are overlapping in their error ranges, with the exception of the Arctic Ocean region (2005–2020: -0.014 ± 0.004 ng m^{-3} yr^{-1}; 1996–2022: -0.007 ± 0.002 ng m^{-3} yr^{-1}). The area-weighted NH average trend in the 2005–2020 calculation is -0.015 ± 0.006 ng m^{-3} yr^{-1}, slightly more negative but overlapping with the trend calculated in the main paper (-0.011 ± 0.006 ng m^{-3} yr^{-1}). Overall, our conclusions remain the same that the NH Hg^0 concentrations are declining between 2005 and 2020 and would be difficult to reconcile with increasing NH anthropogenic emissions.

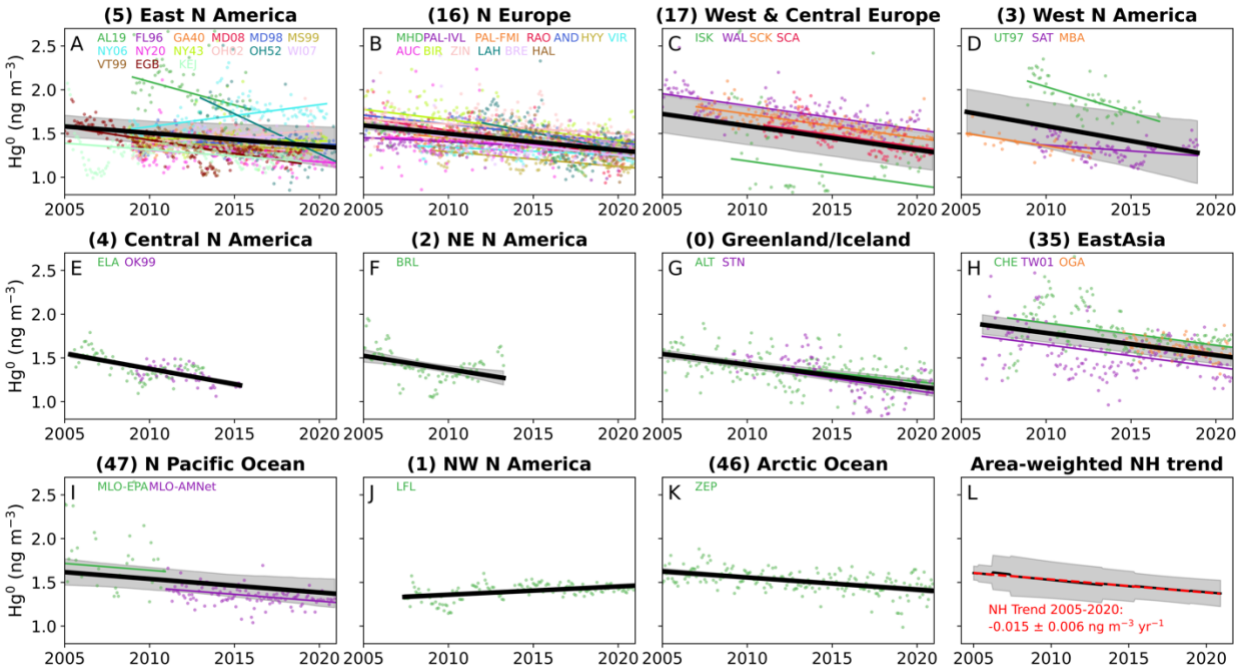

Figure S5. Similar to Fig. 2 but only for the period of 2005–2020, trends in observed gaseous elemental mercury (Hg^0) aggregated by the regions (*A*–*K*) in Fig. 1 (labelled by region number). Trends are calculated with linear mixed effects modeling, with overall regional trends shown in black and shading shows the 5th to 95th percentile range. Individual site deseasonalized monthly means are shown as colored points and individual regressions as colored lines. The overall Northern Hemisphere (NH) trend (*L*) is calculated by taking the area-weighted average of regional trends, with the shading showing the 2σ averaging error. The red dashed curve in *L* is the linear regression trend for 2005–2020, with trend error representing 2σ error from resampling regional trends within their error bounds.

Table S3. Tabulated overall regional trends (± 2σ) calculated through linear mixed effects modelling after restricting site data to 2005–2020 period only. See Table S2 for trends calculated using all data.

Region name (number)	Number of sites	Area (10^6 km^2)	Trend (ng m^{-3} yr^{-1})	Time period
Eastern North America (5)	15	5.69	-0.015 ± 0.015	2005–2020
Northern Europe (16)	12	5.00	-0.019 ± 0.006	2005–2020
West & Central Europe (17)	4	3.79	-0.027 ± 0.005	2005–2020
Western North America (3)	3	3.14	-0.034 ± 0.025	2005–2018
Central North America (4)	2	2.93	-0.035 ± 0.007	2005–2015
Northeastern North America (2)	1	7.66	-0.031 ± 0.016	2005–2013
Greenland/Iceland (0)	2	4.77	-0.025 ± 0.008	2005–2020
East Asia (35)	3	9.46	-0.025 ± 0.006	2006–2020
North Pacific Ocean (47)	1	51.61	-0.015 ± 0.011	2005–2020
Northwestern North America (1)	1	7.51	0.009 ± 0.003	2007–2020
Arctic Ocean (1)	1	6.35	-0.014 ± 0.004	2005–2020
Northern Hemisphere (NH) area-weighted average	**45**		**-0.015 ± 0.006**	**2005–2020**

Section S4. Calculating EAME equations from the GBC box model and perturbation analysis

We followed the approach of Selin (15) to calculate parameters from the EAME equation (Eq. 2) using pulse simulations in the Hg Global Biogeochemical Box model (GBC) (16, 17). We introduced an atmospheric Hg pulse of 100 Mg in the year 2010 and monitored the evolution of legacy re-emissions for 100 years, until 2110 (Fig. S6). The two-term exponential model fits the behaviour of the box model very well (R^2~0.99) on the 100-year time period of the simulation. This fitting reduces the ~40 parameters of the GBC model to 4 understandable parameters, as well as reducing the computation time for legacy re-emissions. We performed a similar experiment by modeling the release of a riverine pulse, and evaluated changes to legacy re-emissions. This equation will differ from the atmospheric pulse, as different timescales are involved (river transport *versus* deposition to oceans) and only a fraction of the riverine pulse will reach the open ocean and not be buried on the coastal shelf.

To estimate a reasonable range in the legacy re-emission pulse parameters (Eq. 2), we performed 1000 parameter perturbation simulations in the GBC model. The 40 relevant parameters that we varied are 35 rate coefficients, 3 parameters for the designation of deposition into soil pools, 1 parameter for geogenic emissions, and 1 parameter for the fraction of riverine particulate Hg reaching the open ocean. These parameters were perturbed simultaneously by factors varying between 0.5 and 2, with Latin Hypercube sampling (18) used to ensure that the parameter space is better explored. For each of the 1000 experiments, we calculated the legacy re-emission pulse parameters (Eq. 2) and selected the 5th–95th percentile of each parameter as the range for simulations in the 3-box atmospheric model (Table S4). The 1000 experiments were conducted twice, once for atmospheric pulses and once for riverine pulses. The code for conducting sensitivity experiments in the GBC model is available here: https://github.com/arifein/gbc-boxmodel-sensitivity.

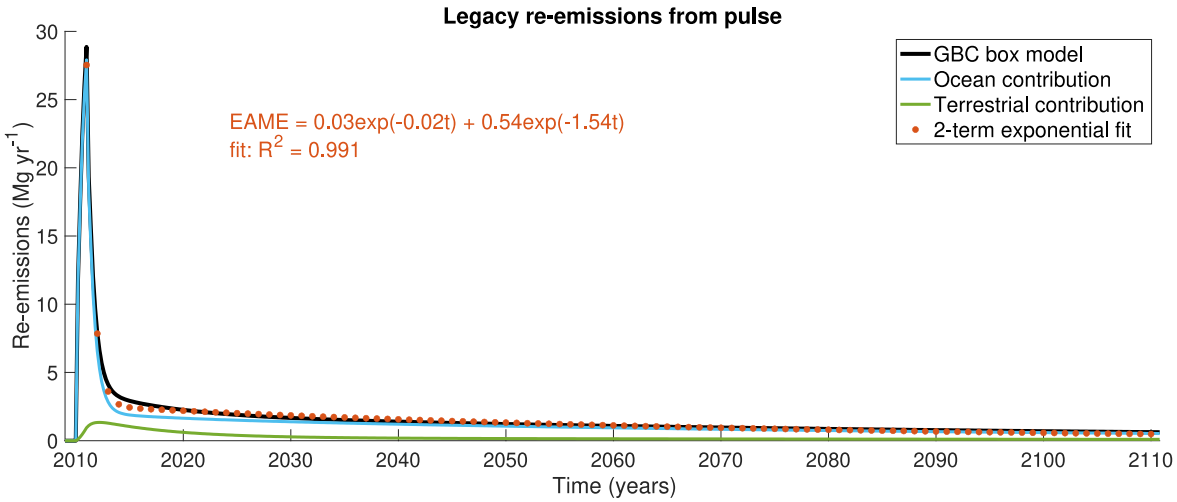

Figure S6. Example of fitting the GBC model pulse experiment to Eq. 2. The contribution of ocean and terrestrial legacy re-emissions to the total are shown as blue and green lines.

Section S5. 3-box atmospheric model parameter variations

The bounds for the 19 parameters that were varied in the 2 × 10^5 simulations, along with their justifications, are listed in Table S4. We sampled the fraction of Hg emitted in the short timescale (f_{short}) and the total re-emissions (E_{total}) instead of directly sampling coefficients a_1 and a_2 in Eq. 2. This is less likely to lead to unrealistic combinations of the *a* coefficients and the *b* lifetimes. Integrating Eq. 2 between time 0 and infinity yields an equation for E_{total}:

$$E_{\text{total}} = a_1 b_1 + a_2 b_2 \qquad \text{(Eq. S2)}$$

The fraction of Hg emitted in the short timescale is equal to:

$$f_{\text{short}} = \frac{a_1 b_1}{a_1 b_1 + a_2 b_2} = \frac{a_1 b_1}{E_{\text{total}}} \qquad \text{(Eq. S3)}$$

We calculated the *a* coefficients from the sampled variables (b_1, b_2, f_{short}, E_{total}) using Eq. S4 and Eq. S5:

$$a_1 = \frac{E_{\text{total}}\, f_{\text{short}}}{b_1} \qquad \text{(Eq. S4)}$$

$$a_2 = \frac{E_{\text{total}}\, (1 - f_{\text{short}})}{b_2} \qquad \text{(Eq. S5)}$$

221 **Table S4**. Bounds of parameters varied for the 2005–2020 simulations in the 3-box atmospheric model.

Parameter	Min	Max	Units	Comment/References
Atmospheric Hg lifetime	3	8	months	Horowitz et al. (19); Parrella et al. (20); Zhang et al. (21)
Error in 1970 emissions and releases	-20	+40	%	Error range suggested for 2000, 2010, 2015 emissions in Streets et al. (22)
Error in 1980 emissions and releases	-20	+40	%	Error range suggested for 2000, 2010, 2015 emissions in Streets et al. (22)
Error in 1990 emissions and releases	-20	+40	%	Error range suggested for 2000, 2010, 2015 emissions in Streets et al. (22)
Error in 2000 emissions and releases	-20	+40	%	Error range suggested for 2000, 2010, 2015 emissions in Streets et al. (22)
Error in 2010 emissions and releases	-20	+40	%	Error range suggested for 2000, 2010, 2015 emissions in Streets et al. (22)
Legacy short lifetime (b_1) (atmospheric pulse)	5.7	14.6	months	Based on perturbation analysis of Amos et al. (16, 17) GBC model (Section S4)
Legacy long lifetime (b_2) (atmospheric pulse)	28.6	96.9	years	Based on perturbation analysis of Amos et al. (16, 17) GBC model (Section S4)
Legacy fraction emitted in short timescale (atmospheric pulse)	7	31	%	Based on perturbation analysis of Amos et al. (16, 17) GBC model (Section S4)
Total re-emissions from initial pulse (atmospheric pulse)	79	379	%	Based on perturbation analysis of Amos et al. (16, 17) GBC model (Section S4)
Legacy short lifetime (b_1) (riverine pulse)	1.6	9.5	months	Based on perturbation analysis of Amos et al. (16, 17) GBC model (Section S4)
Legacy long lifetime (b_2) (riverine pulse)	1	116.9	years	Based on perturbation analysis of Amos et al. (16, 17) GBC model (Section S4)
Legacy fraction emitted in short timescale (riverine pulse)	5	55	%	Based on perturbation analysis of Amos et al. (16, 17) GBC model (Section S4)
Total re-emissions from initial pulse (riverine pulse)	2	160	%	Based on perturbation analysis of Amos et al. (16, 17) GBC model (Section S4)
Difference in percent Hg^0 emitted from anthropogenic sources between 2020 and 2005	-20	20	%	The speciation of emissions in longest available inventory (23) varied by 15% (from 60% Hg^0 in 1970 to 75% Hg^0 in 2010)
Anthropogenic emissions trend in Northern Hemisphere (NH)	-70	70	Mg yr^{-2}	Covers wide range without 2020 emissions becoming negative
Anthropogenic emissions trend in Southern Hemisphere (SH)	-10	10	Mg yr^{-2}	Covers wide range without 2020 emissions becoming negative
Deviation of releases trend from emissions trend in NH	-80	80	Mg yr^{-2}	For example, if NH emissions trend is 30 Mg yr^{-2}, the NH releases trend ranges between -21 and 139 Mg yr^{-2} *
Deviation of releases trend from emissions trend in NH	-35	35	Mg yr^{-2}	For example, if SH emissions trend is -10 Mg yr^{-2}, the SH releases trend ranges between -45 and 25 Mg yr^{-2} †

222 * In the NH, decadal release trends in Streets et al. (24) are 1.97 × emissions trends ± 80
223 † In the SH, decadal release trends in Streets et al. (24) are 1.03 × emissions trends ± 35
224

Fig. S7 visualizes the results of the box model simulations by comparing inputted trends in NH emissions with simulated trends in NH Hg^0 over 2005–2020. Fig. S7A displays the relationship between total NH emissions trends (anthropogenic + legacy) and the Hg^0 trend. The NH total emissions trends that would be compatible with the observed Hg^0 trends (grey range in Fig. S7A) ranges from -15 Mg yr^{-2} to more than -80 Mg yr^{-2}. The relationship between the total emissions trends and the Hg^0 trend crosses close to the origin, meaning that with a zero total emissions trend the simulated median Hg^0 trend is negligible. However, in the case of the anthropogenic emissions trend plot (Fig. S7B), a zero trend in NH anthropogenic emissions will still lead to a positive Hg^0 trend due to increasing legacy emissions (25). The NH anthropogenic emissions trend must be below -8 Mg yr^{-2} in order for the NH Hg^0 trend to be negative. Another aspect of Fig. S7 is that relationship between NH Hg^0 trends and anthropogenic emissions trends is associated with larger uncertainties (Fig. S7B) than that of total emissions (Fig. S7A), as evidenced by the larger red error bars in Fig. S7B. The relationship between total NH emissions trends and the NH Hg^0 concentration trend (Fig. S7A) is mainly affected by uncertainties in the atmospheric Hg lifetime, SH emissions, and speciation trends. However, the relationship of anthropogenic NH emissions with Hg^0 concentrations is affected by the uncertain response of legacy emissions to anthropogenic inputs and the trends in releases to water and land that would accompany anthropogenic emissions trends for 2005–2020, leading to larger error bars.

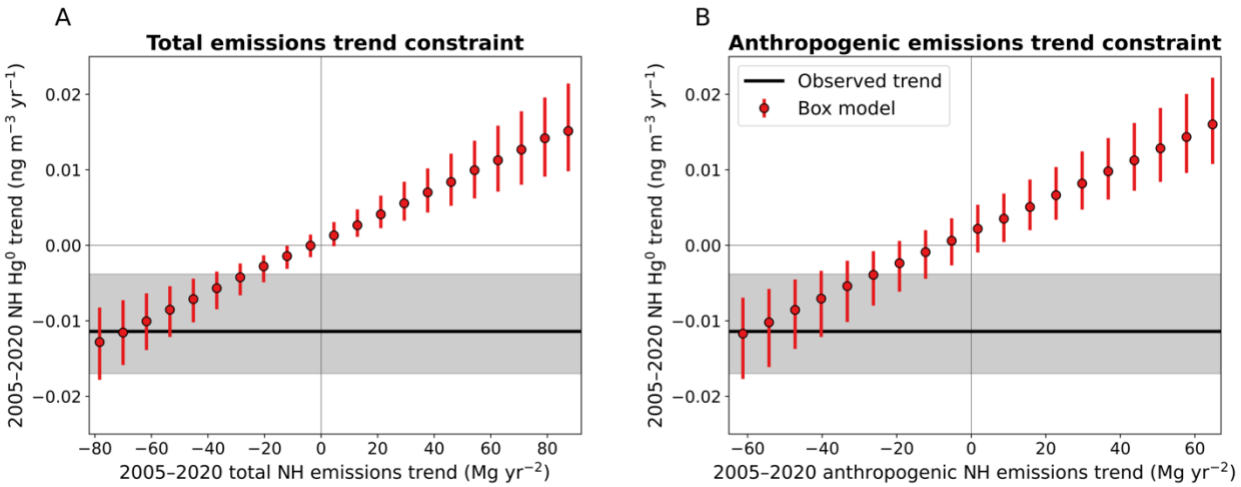

Figure S7. (*A*) Relationship between NH Hg^0 trends and the trends in total NH emissions. The 10^5 box model simulations are summarized in the red points (median) and error bars (5^{th} to 95^{th} percentile). Observed NH TGM trends are shown in the horizontal black line, with the associated error shaded. The overlap between grey shading and red error bars represents the parameter space where the model is compatible with observed trends. (*B*) Relationship between NH Hg^0 trends and trends in anthropogenic NH emissions. Fig. 3A in the main manuscript represents a 1-D representation of these curves for selected values of the anthropogenic NH emissions trend.

The relationships between NH Hg re-emissions trends (2005–2020) and anthropogenic emissions and releases parameters in the 3-box model results are plotted in Fig. S8. We have used Fig. S8F in the main paper to relate the trend in NH anthropogenic emissions from the GEOS-Chem scenarios with the expected NH trend in legacy re-emissions. This relationship was used to identify potential trends in legacy emissions resulting from anthropogenic emissions trends, which can then be incorporated in the GEOS-Chem simulations by scaling ocean Hg^0 concentrations.

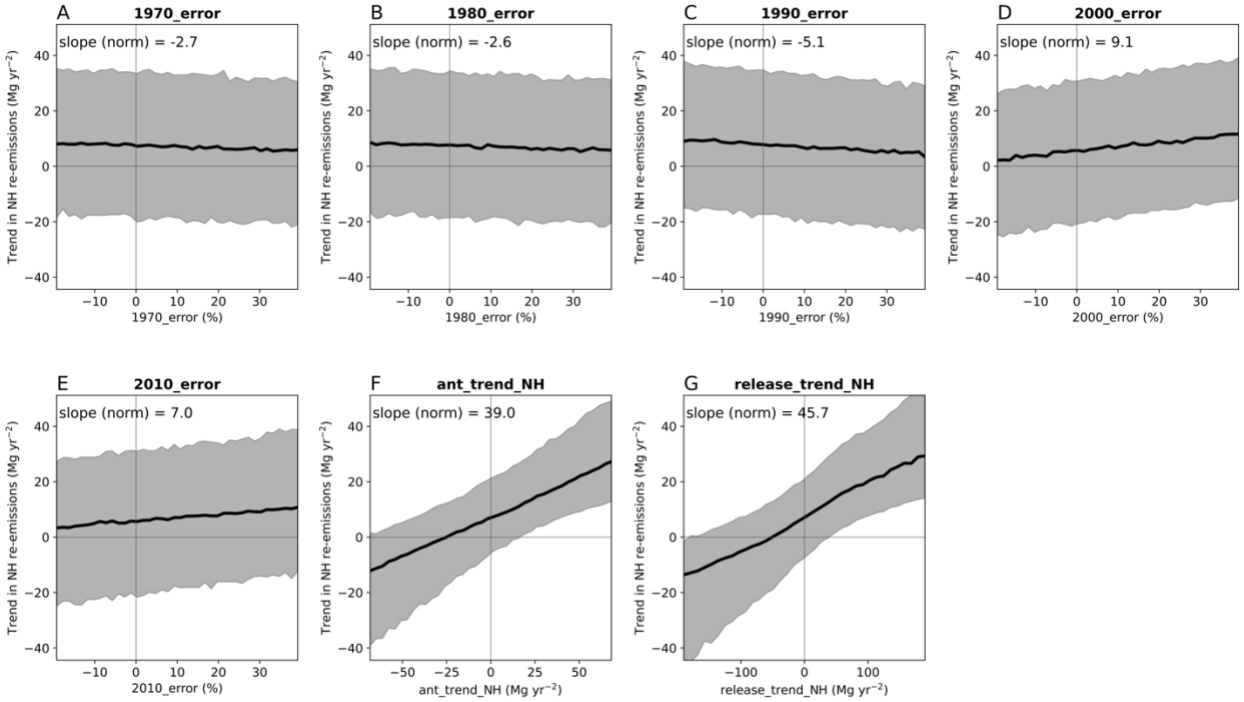

Figure S8. The relationships between Northern Hemisphere (NH) Hg re-emissions trends (2005–2020) and anthropogenic emissions and releases parameters. Plots show the relationship for (*A*) the error in emissions and releases for 1970 in the Streets et al. (24) inventory; (*B*) the error in emissions and releases for 1980; (*C*) the error in emissions and releases for 1990; (*D*) the error in emissions and releases for 2000; (*E*) the error in emissions and releases for 2010; (*F*) the trend in anthropogenic NH emissions for 2005–2020; (*G*) the trend in anthropogenic NH releases for 2005–2020. Black lines show median responses and the shaded area shows the 90% confidence interval (5^{th} to 95^{th} percentile). The slope (normalized to the range of the x-axis parameter) is listed on the plot to illustrate the relative importance of a parameter.

Section S6. Description of GEOS-Chem simulations

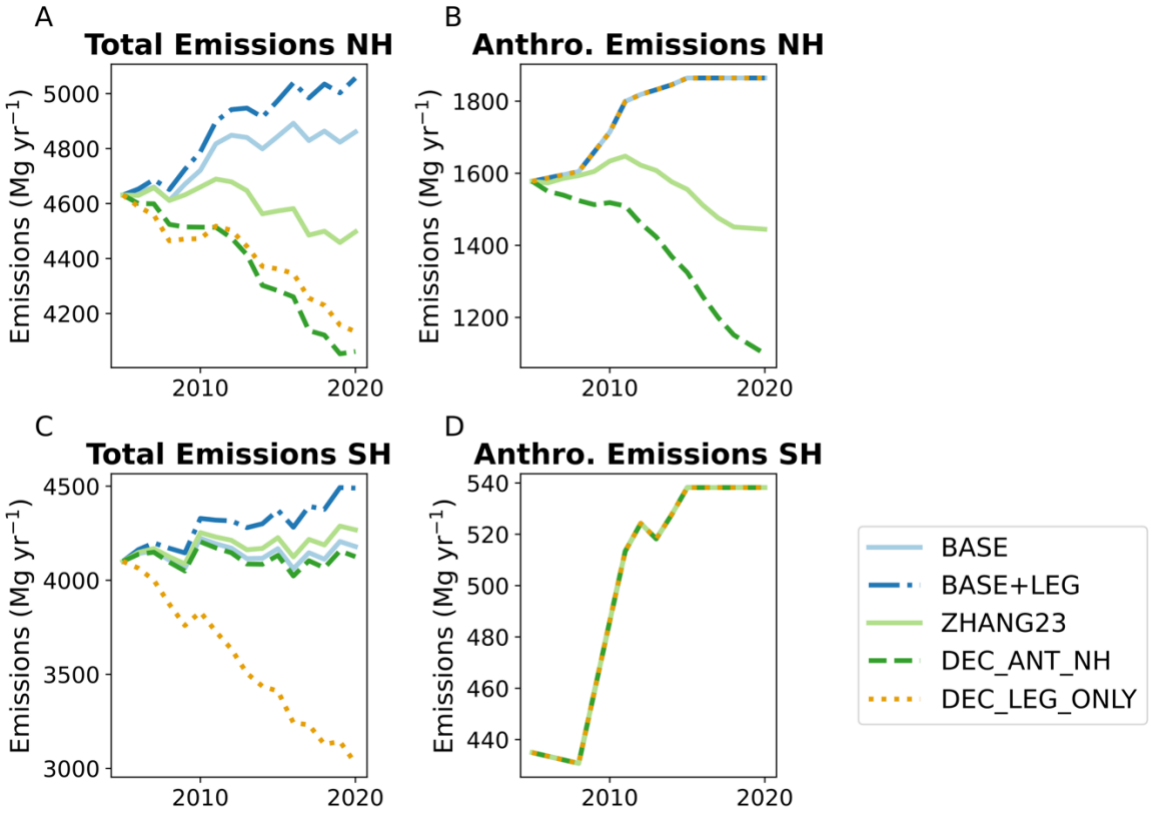

Figure S9. The emission timeseries in GEOS-Chem simulations for 2005–2020: total emissions in the Northern Hemisphere (*A*), anthropogenic emissions in the Northern Hemisphere (*B*), total emissions in the Southern Hemisphere (*C*), and anthropogenic emissions in the Southern Hemisphere (*D*).

Section S7. Dry deposition trend in GEOS-Chem simulations

The Leaf Area Index (LAI) data used in GEOS-Chem comes from a reprocessed version of the Moderate Resolution Imaging Spectroradiometer (MODIS) satellite product (26), and includes the observed interannual variations in vegetation. Our GEOS-Chem simulations thus include the impact of (LAI) variations during 2005–2020 on the dry deposition of Hg^0. The dry deposition scheme of GEOS-Chem and its response to changes in LAI have been thoroughly evaluated against observations by previous studies (27, 28). Here we evaluate the trends in the NH dry deposition of Hg^0 to investigate whether it is a major driver of the Hg^0 trends between 2005–2020.

Figure S10A shows the GEOS-Chem simulated fluxes of dry deposition over the BASE+LEG simulation. The dry deposition flux in the NH increases by 17 Mg yr^{-2} over the simulation, yet this is mainly due to the increasing emissions in the BASE+LEG scenario (+31 Mg yr^{-2} trend over simulation) increasing the amount of Hg^0 in the atmosphere. By dividing the NH Hg^0 burden by the dry deposition flux, we can calculate the dry deposition lifetime in the NH over the simulation (Fig. S10B). One observes a slight decline in the lifetime of Hg^0 dry deposition in the GEOS-Chem simulations over this time period, with a total decline in the lifetime of 3% between 2005 and 2020. Thus GEOS-Chem shows that the NH dry deposition of Hg^0 is indeed becoming faster over this time period, but not to the extent that it would reverse the emission driven changes in Hg^0 (Fig. 3C). Therefore, although it is important to further evaluate the impacts of changing vegetation on Hg cycling and its evolution in the future, during the 2005–2020 time period the dry deposition lifetime trends have a small impact compared to the estimated changes in anthropogenic Hg emissions.

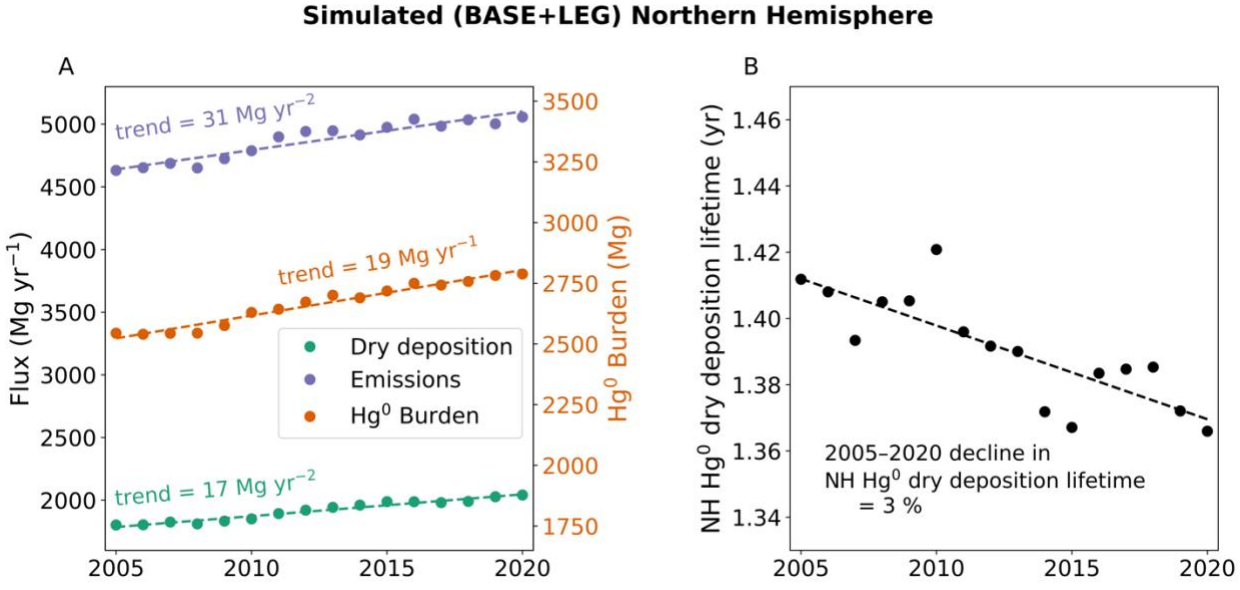

Figure S10. Impacts of changing vegetation on the dry deposition of Hg^0 in the NH. (*A*) Trends in the NH fluxes of dry deposition and total emissions in the BASE+LEG simulation (left y axis), along with changes in the NH Hg^0 burden (right y axis). Linear trend values are listed on the plot. (*B*) Trend in the Hg^0 NH dry deposition lifetime over the simulation, with the relative change between 2005 and 2020 listed on the plot.

Section S8. Additional quantile regression plots

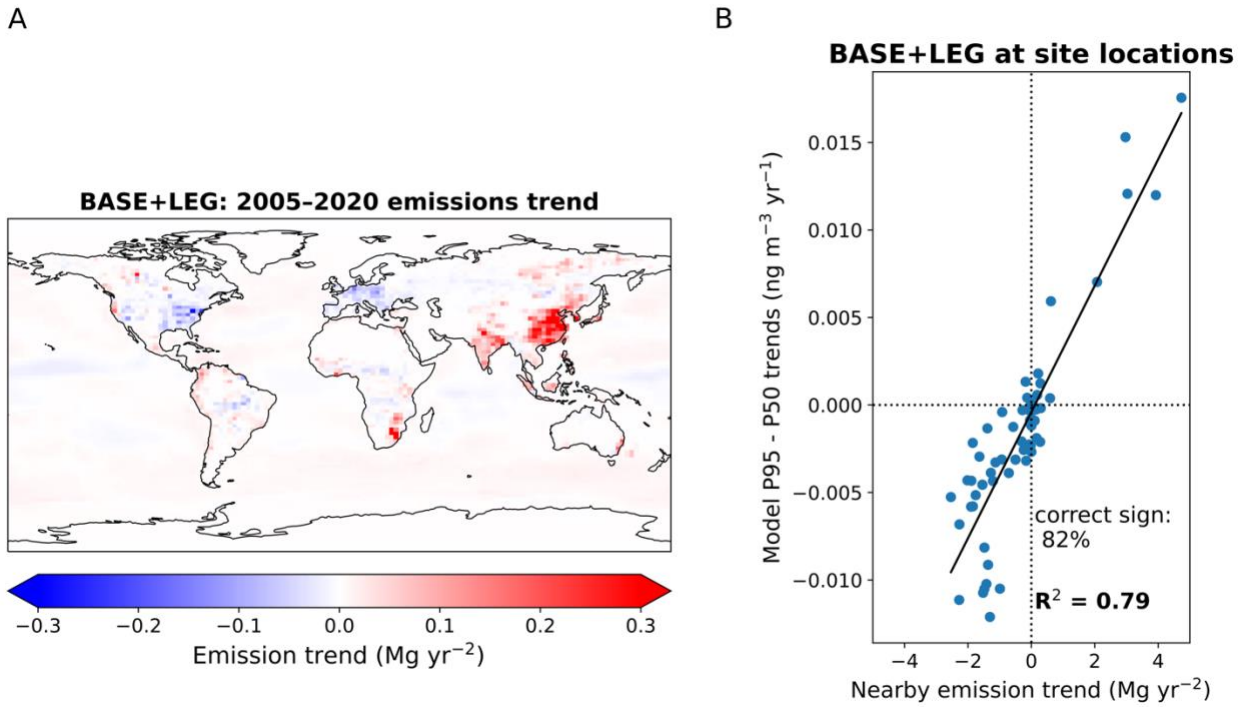

Figure S11. (*A*) Map of the linear trend of Hg emissions in the BASE+LEG simulation between 2005 and 2020. (*B*) Comparing the relationship between the BASE+LEG simulated nearby emission trend and the difference between the 95th percentile (P95) and median (P50) quantile regression Hg^0 trends at grid boxes corresponding to site locations (see Fig. 4C for the full P95 – P50 trends map). The nearby emission trend is calculated by summing emissions trends within two grid boxes (~500 km) of the site location grid box.

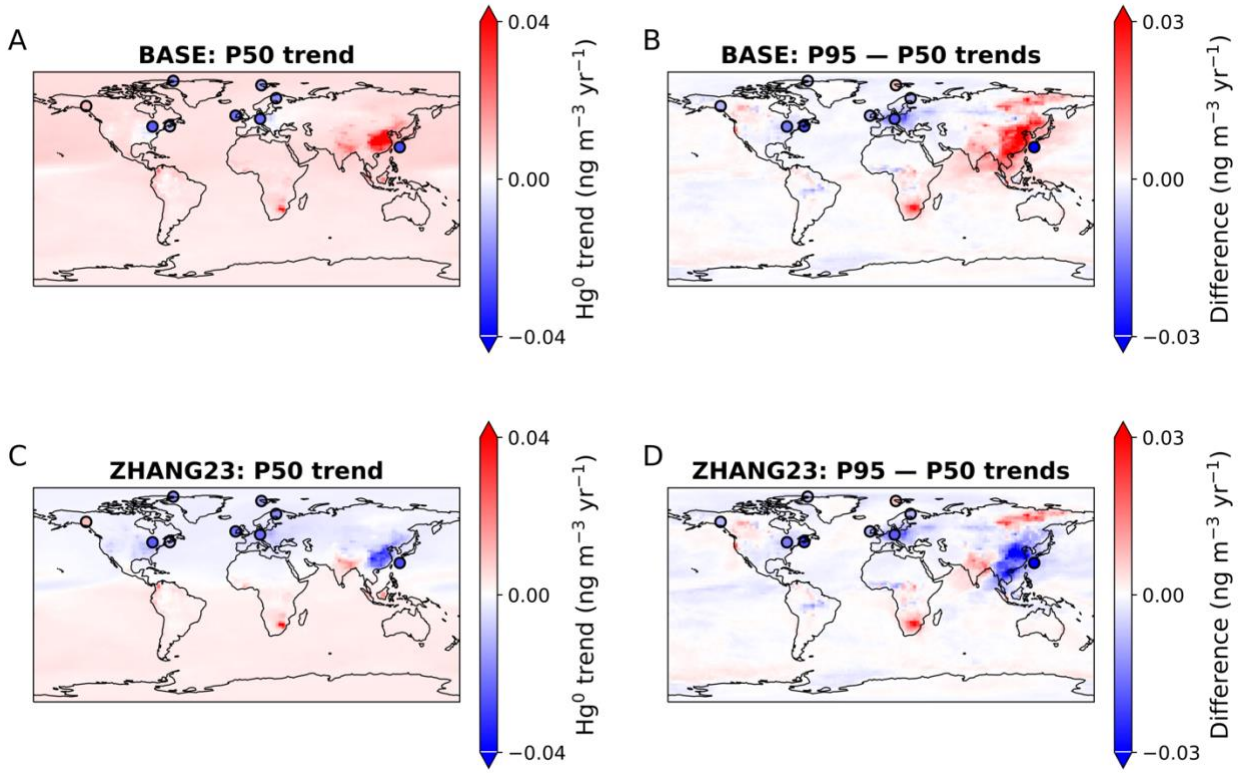

Figure S12. Trend in median (P50) daily deseasonalized simulated values in BASE (*A*) and ZHANG23 (*C*) for each model grid cell. Observed results are plotted in filled circles for 9 stations with more than 13 years of high frequency data. Differences between 95th percentile (P95) trend and median (P50) trend shown for BASE (*B*) and ZHANG23 (*D*) simulations and observations. The other simulations (BASE+LEG, DEC_ANT_NH, and DEC_LEG_ONLY) are shown in Fig. 4.

Section S9. Additional comparisons between observations and model simulations

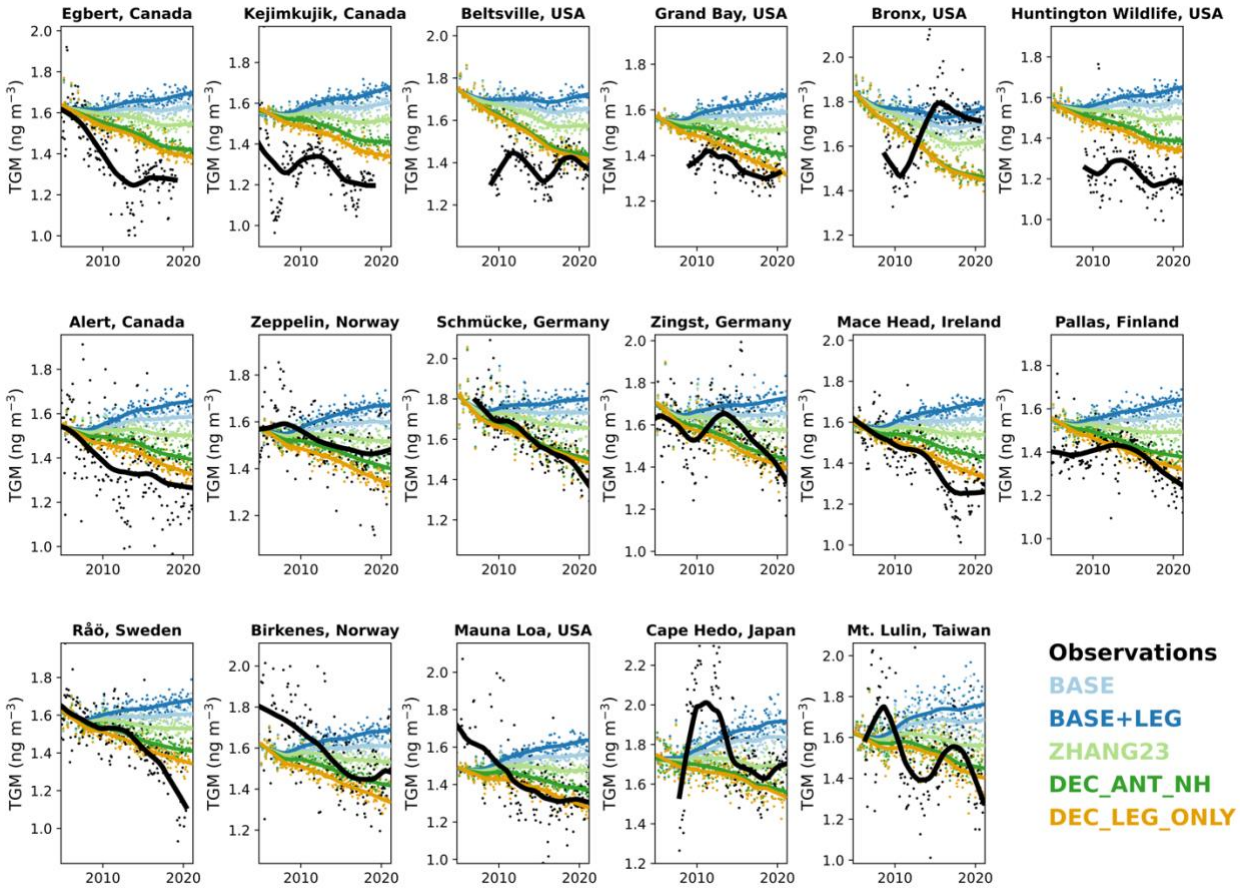

Figure S13. Timeseries plots comparing model simulations (colors) and observations (black) at stations with more than 12 years of data during 2005–2020. Markers show deseasonalized monthly means and lines show the smoothed tendency of the time series calculated using LOWESS (locally weighted scatterplot smoothing) regression.

Section S10. EDGAR v8.1_toxHg emissions inventory

A new anthropogenic emissions inventory has recently been released for 1970–2022, the EDGAR v8.1_toxHg inventory (29). Compared to the previous iteration of this inventory (EDGAR v4.tox2) (23), the v8.1 inventory includes updated spatial proxies and emissions factors and is extended to 2020. The released speciation maps (Hg^0, Hg^{2+}, Hg^P) from the inventory were still in draft form at the time of this manuscript, so we did not run GEOS-Chem simulations with v8.1_toxHg, though this will be upcoming in the MCHgMAP project (30). The total Hg emissions maps have been released in definitive form at this time, so we have analyzed the trends in the total emissions (Fig. S14). The NH trend between 2005 and 2020 is 35 Mg yr^{-2}, very similar to the Streets et al. (22) 2005–2015 trend (34 Mg yr^{-2}). Therefore, our modelling results using the Streets et al. (22) emissions trends are likely applicable to the new EDGAR v8.1_toxHg inventory as well. Increasing global and NH emissions are a common feature in both Streets et al. (22) and EDGAR v8.1_toxHg inventories, in contrast to the observed decline in Hg^0 concentrations.

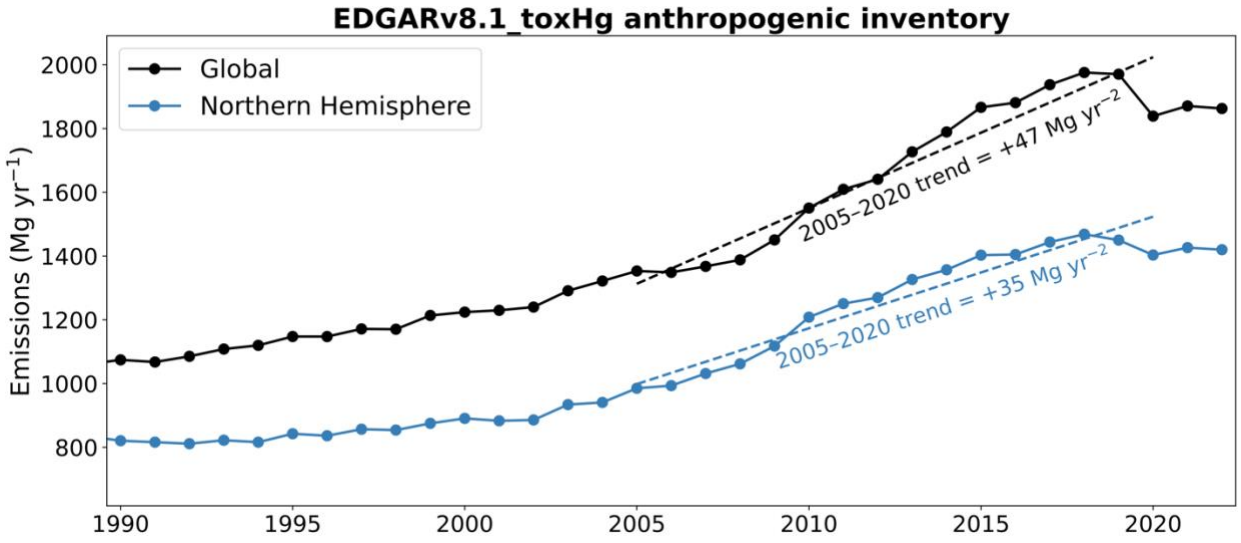

Figure S14. Anthropogenic emissions trend from the EDGARv8.1_tox anthropogenic inventory, with linear trends calculated and plotted for the 2005–2020 period.

Supplementary References

1. M. Iturbide, *et al.*, An update of IPCC climate reference regions for subcontinental analysis of climate model data: definition and aggregated datasets. *Earth Syst. Sci. Data* **12**, 2959–2970 (2020).
2. D. A. Gay, *et al.*, The Atmospheric Mercury Network: measurement and initial examination of an ongoing atmospheric mercury record across North America. *Atmos. Chem. Phys.* **13**, 11339–11349 (2013).
3. F. Carbone, *et al.*, Sea surface temperature variation linked to elemental mercury concentrations measured on Mauna Loa. *Geophys. Res. Lett.* **43**, 7751–7757 (2016).
4. F. Sprovieri, *et al.*, Atmospheric mercury concentrations observed at ground-based monitoring sites globally distributed in the framework of the GMOS network. *Atmos. Chem. Phys.* **16**, 11915–11935 (2016).
5. A. Cole, *et al.*, A Survey of Mercury in Air and Precipitation across Canada: Patterns and Trends. *Atmosphere* **5**, 635–668 (2014).
6. V. L. St. Louis, *et al.*, Atmospheric Concentrations and Wet/Dry Loadings of Mercury at the Remote Experimental Lakes Area, Northwestern Ontario, Canada. *Environ. Sci. Technol.* **53**, 8017–8026 (2019).

7. K. Tørseth, *et al.*, Introduction to the European Monitoring and Evaluation Programme (EMEP) and observed atmospheric composition change during 1972–2009. *Atmos. Chem. Phys.* **12**, 5447–5481 (2012).
8. L. S. P. Nguyen, G.-R. Sheu, D.-W. Lin, N.-H. Lin, Temporal changes in atmospheric mercury concentrations at a background mountain site downwind of the East Asia continent in 2006–2016. *Science of The Total Environment* **686**, 1049–1056 (2019).
9. K. Marumoto, *et al.*, Long-Term Observation of Atmospheric Speciated Mercury during 2007–2018 at Cape Hedo, Okinawa, Japan. *Atmosphere* **10**, 362 (2019).
10. Y. Zhang, *et al.*, Observed decrease in atmospheric mercury explained by global decline in anthropogenic emissions. *Proc. Natl. Acad. Sci. U.S.A.* **113**, 526–531 (2016).
11. K.-L. Chang, *et al.*, Trend detection of atmospheric time series. *Elementa: Science of the Anthropocene* **9**, 00035 (2021).
12. S. N. Wood, Fast stable restricted maximum likelihood and marginal likelihood estimation of semiparametric generalized linear models. *Journal of the Royal Statistical Society (B)* **73**, 3–36 (2011).
13. K.-L. Chang, M. G. Schultz, G. Koren, Selke, Niklas, Guidance note on best statistical practices for TOAR analyses. Available at: https://doi.org/10.48550/arXiv.2304.14236. (2023).
14. P. S. Weiss-Penzias, *et al.*, Trends in mercury wet deposition and mercury air concentrations across the U.S. and Canada. *Science of The Total Environment* **568**, 546–556 (2016).
15. N. E. Selin, A proposed global metric to aid mercury pollution policy. *Science* **360**, 607–609 (2018).
16. H. M. Amos, D. J. Jacob, D. G. Streets, E. M. Sunderland, Legacy impacts of all-time anthropogenic emissions on the global mercury cycle. *Global Biogeochem. Cycles* **27**, 410–421 (2013).
17. H. M. Amos, *et al.*, Global Biogeochemical Implications of Mercury Discharges from Rivers and Sediment Burial. *Environ. Sci. Technol.* **48**, 9514–9522 (2014).
18. M. D. McKay, R. J. Beckman, W. J. Conover, Comparison of Three Methods for Selecting Values of Input Variables in the Analysis of Output from a Computer Code. *Technometrics* **21**, 239–245 (1979).
19. H. M. Horowitz, *et al.*, A new mechanism for atmospheric mercury redox chemistry: implications for the global mercury budget. *Atmos. Chem. Phys.* **17**, 6353–6371 (2017).
20. J. P. Parrella, *et al.*, Tropospheric bromine chemistry: implications for present and pre-industrial ozone and mercury. *Atmos. Chem. Phys.* **12**, 6723–6740 (2012).
21. Y. Zhang, *et al.*, An updated global mercury budget from a coupled atmosphere-land-ocean model: 40% more re-emissions buffer the effect of primary emission reductions. *One Earth* **6**, 316–325 (2023).
22. D. G. Streets, *et al.*, Global and regional trends in mercury emissions and concentrations, 2010–2015. *Atmospheric Environment* **201**, 417–427 (2019).
23. M. Muntean, *et al.*, Evaluating EDGARv4.tox2 speciated mercury emissions ex-post scenarios and their impacts on modelled global and regional wet deposition patterns. *Atmospheric Environment* **184**, 56–68 (2018).
24. D. G. Streets, *et al.*, Five hundred years of anthropogenic mercury: spatial and temporal release profiles. *Environ. Res. Lett.* **14**, 084004 (2019).
25. H. Angot, *et al.*, Global and Local Impacts of Delayed Mercury Mitigation Efforts. *Environ. Sci. Technol.* **52**, 12968–12977 (2018).
26. H. Yuan, Y. Dai, Z. Xiao, D. Ji, W. Shangguan, Reprocessing the MODIS Leaf Area Index products for land surface and climate modelling. *Remote Sens. Environ.* **115**, 1171–1187 (2011).
27. A. Feinberg, T. Dlamini, M. Jiskra, V. Shah, N. E. Selin, Evaluating atmospheric mercury (Hg) uptake by vegetation in a chemistry-transport model. *Environ. Sci.: Processes Impacts* **24**, 1303–1318 (2022).
28. A. Feinberg, M. Jiskra, P. Borrelli, J. Biswakarma, N. E. Selin, Deforestation as an Anthropogenic Driver of Mercury Pollution. *Environ. Sci. Technol.* **58**, 3246–3257 (2024).
29. M. Muntean, *et al.*, EDGAR v8.1 Global Mercury Emissions. European Commission, Joint Research Centre (JRC) [Dataset] PID: http://data.europa.eu/89h/83b507d7-5218-4dc5-95f9-0ec36f073204. Deposited 2024.
30. A. Dastoor, *et al.*, The Multi-Compartment Hg Modeling and Analysis Project (MCHgMAP): Mercury modeling to support international environmental policy. *Geoscientific Model Development Discussions* **2024**, 1–171 (2024).